Energy Conversion and Management 284 (2023) 116979

Contents lists available at ScienceDirect

Energy Conversion and Management

journal homepage: www.elsevier.com/locate/enconman

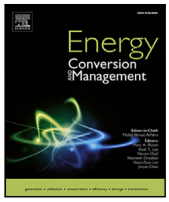

Design of a carbon capture system for oxy-fuel combustion in compression ignition engines with exhaust water recirculation

J.M. Luján, F.J. Arnau *, P. Piqueras, V.H. Farias

CMT Motores Térmicos, Universitat Politècnica de València, Spain

ARTICLE INFO

Keywords:
Oxy-fuel combustion
Internal combustion engine
Membrane
MIEC
Energy recovery
Carbon capture
Water recirculation
Zero emissions

ABSTRACT

The oxy-fuel combustion engine concept with onboard oxygen generation and carbon capture (CC) is studied using as a starting point a baseline oxy-fuel combustion layout coupled to a mixed ionic-electronic conducting membranes for producing oxygen (O_2) from the air. A CC system is designed accounting for the flash-out temperatures and the operating pressure of the last CO_2 purification step. The proposed engine concept is optimized through the product of useful effective efficiency and engine brake power,which is maximized actuating on the start of injection (SOI) for every assessed gas path layouts. The additional cooling power required by the carbon capture system (CC) is also contemplated . Initially, two approaches are compared when the CC is coupled to the O_2 generation unit, including or not an intake cooler. The use of intake cooler yields better engine performance than removing it but increases the cooling power requirements significantly. The extreme results from using or not the intake cooler, indicates that a proper solution could combine both cases, approaching for a different cooling concept. A mixer model is developed to recirculate part of the water condensed in the CC towards the cylinder inlet to lower the intake gas temperature and increase the oxidizer heat capacity ratio. From this layout, an optimum setup for SOI and recirculated water mass flow is found considering the trade-off between additional cooling power and engine performance. Indeed, this case reduces the total ICE additional cooling power required by the exclusive use of an intake cooler by about 27% and improves the engine performance by about 20% in comparison to the lack of intake cooling of the charge flow.

1. Introduction

In recent years, climate change has gradually become a major concern as a result of emissions of greenhouse gases (GHG), especially carbon dioxide (CO_2) [1]. Road transport represents more than 70% of all GHG emissions from the mobility industry, responsible for almost 25% of Europe's GHG [2] with a conventional passenger vehicle emitting almost 4.6 metric tons of CO_2 per year [3]. Therefore, solutions to mitigate the environmental impact of internal combustion engines (ICEs) on global warming are claimed, such as developing systems with low or zero tank-to-wheel emissions [4,5] and promoting the use of e-fuels (synthetic fuel with low environmental impact) [6,7]. In such a context, the oxy-fuel combustion may be considered as a suitable solution to reduce and possibly eliminate CO_2 emissions as well as other pollutants in ICE such as nitrogen oxides (NO_x), carbon monoxide (CO) and hydrocarbons (HC) [8].

The oxy-fuel combustion technology uses pure oxygen blended with recirculated flue gas, instead of air, to react with fuel for the combustion. Currently, the oxy-fuel combustion concept has been chiefly applied to large-scale power plants for reducing the CO_2 emissions, but at the cost of penalizing the process thermal efficiency [9]. Furthermore, its potential application is evaluated for cement production [10], the refining industry [11], and biomass-fired power plants [12]. Concerning ICEs, the oxy-fuel combustion concept may be applied to them along with exhaust gas recirculation (EGR), composed mainly of water vapor and CO_2, to reduce the maximum in-cylinder temperature during the combustion process [13], since the combustion process takes place under highly oxygen-enriched environment. Also, once no nitrogen is present in this combustion concept, the NO_x emissions may be completely eradicated. Consequently, the combustion process may be performed without the trade-off between NO_x and other pollutants emissions [14]. Thus, the engine may be operated with lean burn combustion [15], which may significantly reduce soot and CO emissions, and thereby, H_2O and CO_2 are the major combustion products.

Many research works have emerged to study strategies for controlling the combustion process in oxy-fuel ICEs since that is critical for minimizing emissions and maximizing thermal efficiency and power

* Corresponding author.
E-mail address: farnau@mot.upv.es (F.J. Arnau).

https://doi.org/10.1016/j.enconman.2023.116979
Received 2 January 2023; Received in revised form 20 March 2023; Accepted 27 March 2023

Nomenclature

Abbreviations

BSFC	Brake Specific Fuel Consumption
CAD	Crank Angle Degree
CC	Carbon Capture
CI	Compression Ignition
EGR	Exhaust Gas Recirculation
EOS	Equation of State
Exp	Experimental Data
GHG	Greenhouse Gas Emission
HE	Heat Exchanger
HEN	Heat Exchange Network
ICE	Internal Combustion Engine
MIEC	Mixed Ionic-Electronic Conducting Membrane
Mod	Model Data
OC	Oxidation Catalyst
PID	Proportional–Integral–Derivative Controller
PR	Peng–Robinson
RK	Redlich–Kwong
SI	Spark Ignition
SOI	Start of Injection
SRK	Soave–Redlich–Kwong
TF	Flash Outlet Temperature
VEMOD	Virtual Engine Model
VGT	Variable Geometry Turbocharger
VLE	Vapor–Liquid Equilibrium
WIC	With a Cooler before Intake Manifold
WIR	With Water Recirculation
WMF	Water Mass Flow
WOC	Without a Cooler before Intake Manifold
WOR	Without Water Recirculation

Variables

γ	Heat capacity ratio
λ	Oxygen–fuel Equivalence Ratio
ω	Acentric Factor
ϕ	Fugacity Coefficient
σ, ε, Ω, Ψ	Constants for Cubic Equations of State
ζ	Vapor Mole Ratio
c_p	Specific Heat Capacity at Constant Pressure
F	Molar Flow
h	Specific Enthalpy
k_{ij}	Binary Interaction Parameter between species i and j
n	Number of Components
P	Pressure
R	Universal gas constant
T	Temperature
v	Molar Volume
x	Liquid Mole Fraction
y	Vapor Mole Fraction
z	Overall Mole Fraction

Subscript

0	Reference Condition
c	Critical Point
dew	Dew Point
i	Component i
in	Inlet Condition
liq	Liquid Phase
out	Outlet Condition
r	Reduced Variable
vap	Vapor Phase

performance [16,17]. Thus, vital operating parameters have been analyzed at experimental and simulation levels in oxy-fuel compression ignition (CI) and spark ignition (SI) engines: EGR [18,19], water injection [20], compression ratio [21] and supplement fuel [22]. For instance, water injection may be considered a promising technique to control the in-cylinder temperature, improve the combustion phase and, as a consequence, increase engine efficiency [23] since the heat capacity ratio (γ) of water is higher than that of CO_2 in the working fluid [24]. Moreover, Serrano et al. [25] developed an experimentally-validated model to assess the feasibility of oxy-fuel combustion in SI engines. Working with a single-cylinder engine, they concluded that the EGR operating range is strictly narrow (from 60% to 70%) due to the material resistance and combustion stability, and, once no knocking issues are expected, increasing the compression ratio may be an attractive strategy for recovering part of the thermal efficiency reduction at oxy-fuel combustion application. In addition, Arnau et al. [26] applied the oxy-fuel concept to a multi-cylinder SI engine using oxygen transport membranes to produce the oxygen needed by the engine operating requirements. Among the main simulation results, it may be noted that, in general, the oxy-fuel system efficiency is lower if compared to a conventional SI engine, but it is somewhat better at high speeds and high indicated mean effective pressures.

With respect to oxygen production for oxy-fuel combustion, ionic-electronic conducting membranes (MIECs) seem to be a convenient means towards this end due to their energy consumption reduction of 0.5%–9% and economic saving of 10.5–17.5% compared to other oxygen separation methods such as cryogenic air separation [27]. The MIEC transfers oxygen from the feed side towards the permeate one using the partial pressure gradient between both sides as a driving force and high fluid temperatures [28]. Indeed, the MIEC operates in an electric-circuit mode transporting oxygen ions from the feed side to the permeate one, recombining to form oxygen molecules on the membrane surface, and oppositely transferring electrons [29]. Serra et al. [30] carried out a characterization study of oxygen transport in $Ba_{0.5}Sr_{0.5}Co_{0.8}Fe_{0.2}O_{3-\delta}$ (BSCF) MIEC based on an experimental and numerical assessment for evaluating the effects of process variables on the membrane behavior. Their results show that oxygen production performance is improved when the BSCF MIEC is operated at high temperatures (700 °C to 1000 °C) and when CO_2 or H_2O are used as a sweep gas for decreasing the oxygen partial pressure at the permeate side.

One of the most attractive advantages of using oxy-fuel combustion in fossil fuel-based combustion is the possibility of CO_2 capture and storage from the exhaust gas by basically removing water through liquid condensation and compression steps. In addition to reducing greenhouse gas emissions, CO2 capture provides a by-product that offers new opportunities and challenges [31]. Although the combination of CO_2 capture systems with oxy-fuel power plants is an established technology [32,33], the use of such systems in ICEs dedicated to land-based propulsion is still a major challenge. Even more so if such an engine is capable of generating its own oxygen. For instance, Sharma et al. [34] studied the on-board CO_2 capture and storage in ICEs

coupling, via Rankine cycle, a temperature swing adsorption to a turbocharged system to compress and liquefy CO_2 using the exhaust gas thermal energy. According to their exergy and energy analyses, one may see that the proposed system may reduce by 90% the CO_2 emission without energy penalty. In 2009, Bilger et al. [35] investigated the feasibility of using internal combustion Rankine cycle engines for carbon capture (CC) in automotive applications, achieving a significant increase in specific power output and thermal efficiency. Nevertheless, accurate thermodynamic state models for multi-component CO_2 mixtures are essential for the operation and design of processes inside carbon capture and storage context, especially concerning the modeling of separation systems based on volatility difference [36]. Moreover, existing cubic equations of state (EOS), such as Redlich–Kwong (RK) [37], Soave–Redlich–Kwong (SRK) [38] and Peng–Robinson (PR) [39], may be considered a satisfactory way to predict the vapor–liquid phase equilibrium (VLE) for pure compounds and mixtures, giving reasonable results if their binary interaction parameters (k_{ij}) are calibrated with reliable experimental data [40]. Thus, considering the oxy-fuel combustion application for power plants, well-calibrated cubic EOS may be used to model the condensation steps as well as the CO_2 purification process to calculate the amount of CO_2 captured from the exhaust gas and the energy requirements for that purpose with reasonable accuracy.

Finally, the current manuscript aims to continue the work conducted by Serrano et al. [41,42] and Arnau et al. [43] whereby a feasibility study of the oxy-fuel combustion applied to CI engine using oxygen separation membranes was carried out. The heat exchanger- and turbocharging layout, as well as the BSCF MIEC model (the latter based on results obtained by Serra et al. [30] for generating oxygen) are preserved, and a CC system is coupled to the previous model at the tailpipe outlet. As cubic EOSs are more straightforward for calculation procedure than state-of-the-art EOS due to their simple structure, the PR EOS is employed in this project to model the VLE concerned in the CC system with the temperature-dependent binary interaction parameters calibrated with experimental results given by the literature within the operating conditions (temperature, pressure, and composition) of interest for CO_2 capture related to oxy-fuel combustion. In general, the CO_2 capture process chains found in the literature may approximately cover temperatures from 25 °C to 1346 °C and pressures from 0.5 bar to 80 bar [44,45]. The CC system is essentially composed of two intercooled compression steps with intermediate water removal followed by a CO_2 purifier whereby the CO_2 is separated from O_2 when the combustion process is performed in lean combustion conditions. In addition, two flow recirculations are proposed: CO_2+O_2 recirculation to reuse the O_2 excess in the exhaust gas to enhance the net engine power output; and water recirculation to both reduce intake oxidant charge temperature and increase the intake flow water composition and, thereby, the γ of the in-cylinder trapped mass, thus improving the engine thermal efficiency.

The novelty presented in this article is based on the whole picture of the process to highlight the feasibility of this system (membrane-based oxy-fuel combustion with CC for zero-emission power generation) taking into account different systems operating together and their respective submodels. In fact, to the best of the authors' knowledge, this is the first work in which an automotive multi-cylinder engine is modeled with onboard oxygen self-generation (via MIECs using exhaust gas wasted energy) coupled to a carbon capture system with liquid water and surplus vapor recirculations into the engine intake manifold and combustion chambers, respectively.

2. Materials and methods

In this section, the thermodynamic model is calibrated with experimental data to predict the behavior of several elements whereby there is a phase change. Afterward, initial amendments are proposed to the reference oxy-fuel combustion layout in order to check the need for a turbocharger upstream of the intake manifold. Also, a CC model is proposed, finding the best operating conditions in terms of energy requirement and CO_2 purity, and once developed, it is coupled to oxy-fuel combustion layout considering the reuse of the excess of O_2 coming from the CC system. Finally, a water mixer model is proposed to recirculate part of the water condensed in the flashes in order to enhance the engine thermal efficiency and net mechanical power.

Table 1
α-functions and parameters for cubic EOS.

EOS	$\alpha(T_r)$	σ	ε	Ω	Ψ
RK	$T_r^{-1/2}$	1	0	0.08664	0.42748
SRK	$\alpha_{SRK}(T_r,\omega)$	1	0	0.08664	0.42748
PR	$\alpha_{PR}(T_r,\omega)$	$1+\sqrt{2}$	$1-\sqrt{2}$	0.07780	0.45724

$\alpha_{SRK}(T_r,\omega) = \left[1+(0.480+1.574\omega-0.176\omega^2)(1-T_r^{1/2})\right]^2$

$\alpha_{PR}(T_r,\omega) = \left[1+(0.37464+1.574226\omega-0.26992\omega^2)(1-T_r^{1/2})\right]^2$

2.1. Thermodynamic model for VLE

EOS is a thermodynamic approach to relate state variables (pressure, temperature, and volume) and describe the states of a fluid and its properties [46]. Indeed, one of their primary applications is the prediction of the VLE for pure compounds and mixtures considering the non-ideality of the system [47]. In general, conventional EOS, such as RK, SRK, and PR, may be expressed with the following generalized cubic formulation relating pressure (P), temperature (T), and molar volume (v):

$$P = \frac{RT}{v-b} - \frac{a(T)}{(v+\varepsilon b)(v+\sigma b)} \tag{1}$$

For a given EOS, parameters $b = \Omega\frac{RT_c}{P_c}$ and $a(T) = \Psi\frac{\alpha(T_r)R^2T_c^2}{P_c}$ are substance dependent with the temperature dependence of $\alpha(T_r)$ specific to each EOS considering the reduced temperature defined by $T_r = \frac{T}{T_c}$, and the acentric factor (ω), variable for quantifying the centricity of a molecule, and critical pressure (P_c) and temperature (T_c) of each substance. Moreover, σ, ε, Ω and Ψ are pure numbers specific to a particular EOS but independent of the substance. Table 1 summarizes the parameter assignments for each EOS [48].

When predicting the thermodynamic states for mixtures, the EOS for a pure substance may also be applied to them using the concept of a one-fluid mixture. For a mixture with given composition, an equivalent pure-compound behavior regarding temperature and pressure variations is assumed with some parameters adjusted to the mixture composition. Thus, empirical mixing rules are proposed, and some conventional ones may be expressed by Eqs. 2 and (3), where parameters $a(T)$ and b have quadratic and linear, respectively, dependence on mole fraction z with binary parameter k_{ij} calibrated by fitting to experimental data for each pair of substances (ij) [47,48]:

$$a(T) = \sum_{i=1}^{n}\sum_{j=1}^{n} z_i z_j \sqrt{a(T)_i a(T)_j}(1-k_{ij}) \tag{2}$$

$$b = \sum_{i=1}^{n} z_i b_i \tag{3}$$

In addition, the parameter k_{ij} may also be formulated as temperature-dependent regarding the system in question [49]. Furthermore, other exact thermodynamic properties of interest in this work may be derived from EOS, such as fugacity coefficient (ϕ) and specific real enthalpy (h) calculated from a reference condition (0) for a given system [48]:

$$\ln\phi = \int_0^P \left(\frac{Pv}{RT}-1\right) d\ln P \tag{4}$$

$$h = h_0 + \sum_{i=1}^{n} z_i \int_{T_0}^{T} c_{p,i0}\, dT - RT + Pv - \int_{\infty}^{v}\left[P - T\left(\frac{\partial P}{\partial T}\right)_v\right] dv \tag{5}$$

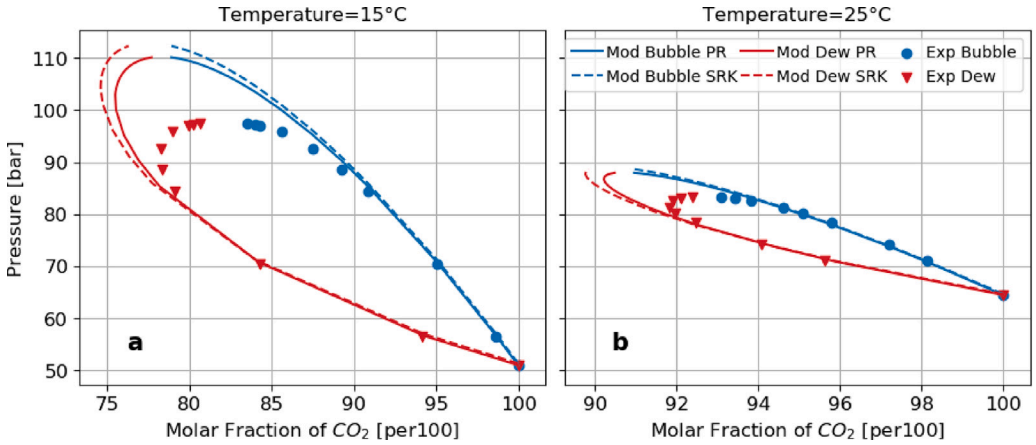

Fig. 1. Phase diagram at constant temperature for the CO_2-O_2 binary system comparing model and experimental data.

Table 2
The best $k_{CO2,O2}$ for PR and SRK EOSs.

	PR	SRK
$k_{CO2,O2}$	0.17431	0.20298

One of the fundamental criteria for achieving the thermodynamic equilibrium between vapor and liquid phases is when species in either a pure or mixture system have the same fugacity in every phase, and thereby, the following condition for each compound is necessary for equilibrium phase [50] considering the vapor and liquid Mole fraction of each specie, y_i and x_i, respectively:

$$y_i\phi_{i,vap} = x_i\phi_{i,liq} \tag{6}$$

Thus, calibration processes of EOS may be performed based on Eq. (6) and, hence, the binary parameters for major pairs of substances within CC and oxy-fuel combustion scenario (CO_2-O_2, O_2-H_2O and CO_2-H_2O) are adjusted with experimental data from the literature. As SRK and PR EOSs are widely used by the industry to simulate VLE behavior of fluids considering the ω of substances [50], and thereby more elaborated than RK, which only predicts the fluid state of a limited range of substances, they are contemplated in this work to model the complex phase change for the CO_2-O_2 binary system. In this case, constant-temperature phase diagrams are built considering 15 °C and 25 °C, which are common ambient temperatures for capturing CO_2 without the need for substantial cooling power. Therefore, k_{CO_2,O_2} is determined by minimizing the sum of squared errors between the model and data for the partial pressure of CO_2 in equilibrium with the bubble point for a given composition as depicted in Fig. 1. The interaction parameter values found using PR and SRK are depicted in Table 2, with PR EOS fitting better the experimental data taken from the work published by Westman et al. [51]. As shown in Fig. 1, these EOSs are not able to predict the critical point with reasonable accuracy; however, both are satisfactory for simulating the VLE within a pressure range (around from 50 bar to 80 bar) whereby the CO_2 may be captured and separated from O_2 at environment temperatures with high purity.

As PR EOS slightly provides better results than SRK in the previous assessment, it is selected and applied to other water-mixture binary systems, such as water-O_2 and water-CO_2, since the binary CO_2-O_2 is the most critical system wherein more elaborated models like cubic EOS are really necessary [52]. Thus, a similar procedure is followed to calibrate the PR EOS for the O_2-H_2O binary (Fig. 2) with experimental data taken from the work published by Stephan et al. [53]. However, in such a study, a k_{O_2,H_2O} value is found for each temperature and, thereby, after a fitting procedure, a temperature-dependent linear function is proposed for the interaction parameter, where the temperature is employed in °C as depicted in Eq. (7). Fig. 2 presents the VLE

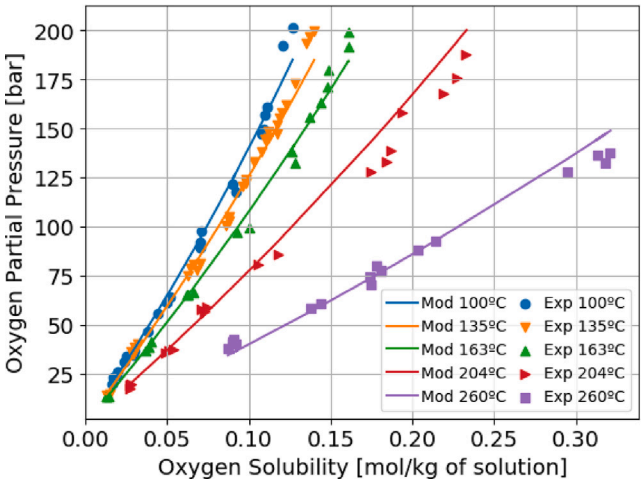

Fig. 2. VLE for the O_2-H_2O binary system comparing model and experimental data. The solution is only composed of water and O_2.

in terms of oxygen solubility in the liquid phase in equilibrium with oxygen partial pressure in the vapor phase. As vapor and liquid phases contain mostly oxygen and water, respectively, system pressure may be approximated by oxygen partial pressure. Therefore, one may see that the proposed model is suitable to predict the VLE at a low-pressure range (around from 15 bar to 125 bar), which is interesting for CC applications, whereas its accuracy is undermined at high-pressure values.

$$k_{O_2,H_2O} = 0.003T - 0.3428 \tag{7}$$

Analogous method is applied to CO_2-H_2O system in order to calibrate its corresponding interaction parameter k_{CO_2,H_2O} for each temperature data, as represented in Fig. 3. In that case, the experimental data for temperatures from 25 °C to 45 °C, and from 100 °C to 200 °C are taken from works published by Valtz et al. [54] and Muller et al. [55], respectively. Thus, a temperature-dependent linear function is also suggested with temperature used in °C as shown in Eq. (8) after a fitting procedure considering phase change data. Experimental data found in literature [54,55] are separated for bubble (Fig. 3a and c) and dew (Fig. 3b and d) pressures, so the left and right experimental points in Fig. 3 are not necessarily in equilibrium for a given CO_2 overall composition and a given temperature, and consequently, bubble and dew points are calculated independently. Although model accuracy is not so satisfactory for low temperatures when the slope of pressure as a function of CO_2 composition appears to be too sharp for dew points,

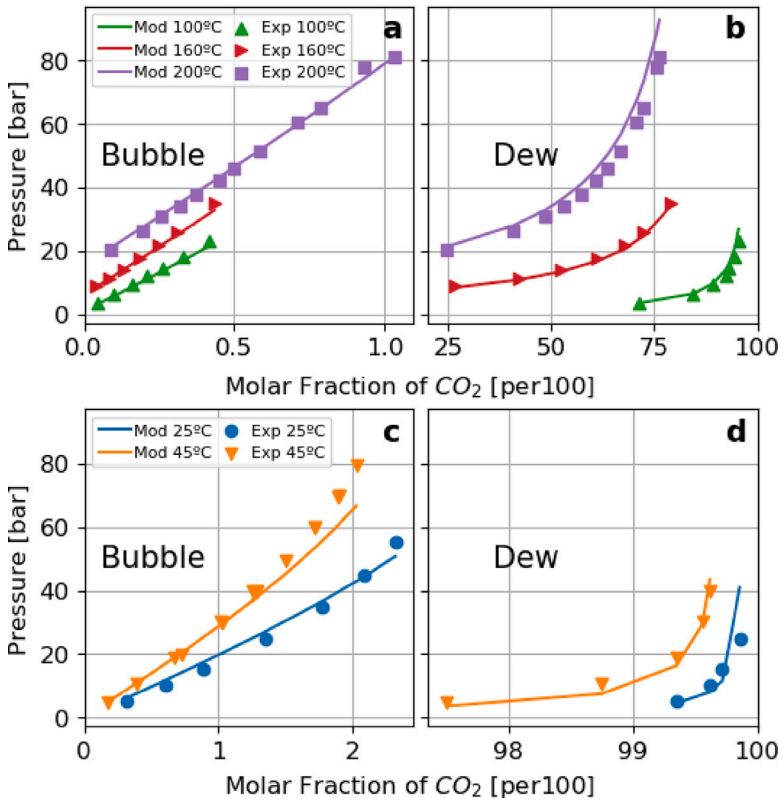

Fig. 3. VLE for the CO_2-H_2O binary system comparing model and experimental data. Left and right plots represent the bubble and dew points, respectively.

it fits the experimental data properly for high temperatures within a broad pressure range considering the CO_2 capture context.

$$k_{CO_2,H_2O} = 0.0009T - 0.1455 \tag{8}$$

Thus, after having the binary parameters calibrated for PR EOS, this thermodynamic approach is applied to simulate the flash processes in this study taking into account the VLE plus mass and energy balances solving a non-linear system with $2n + 2$ equations (Eqs. (6), (9), (10) and (11)) and $2n+2$ unknowns (ζ, y_i, x_i and Q) for given overall mole fraction (z_i), pressure (P), inlet mole flow (F) and inlet and outlet temperatures (T_{in} and T_{out}), assuming vapor and liquid flows are in equilibrium, where n is the number of components, ζ is the vapor mole ratio and Q is the heat exchanged with the surroundings:

$$z_i = \zeta y_i + (1-\zeta)x_i \tag{9}$$

$$\sum_{i=1}^{n} y_i - \sum_{i=1}^{n} x_i = 0 \tag{10}$$

$$Q = F\left[h_{in}(T_{in}, P, z_i) - \zeta h_{vap}(T_{out}, P, y_i) - (1-\zeta)h_{liq}(T_{out}, P, x_i)\right] \tag{11}$$

2.2. Initial amendment to oxy-fuel engine layout

The 2.2 L turbocharged and direct-injection CI engine employed by Serrano et al. [41] and Arnau et al. [43] in previous studies is also used in this work. The baseline engine was calibrated with experimental data for full- and part-load operating points in those cases. Likewise, the in-house software so-called Virtual Engine Model (VEMOD) [56] is used for carrying out thermo-and fluid dynamics calculation of the gas in the CI ICE cycle and the Brayton cycle, wherein the MIEC generates oxygen. The details about the original oxy-fuel combustion engine layout (Fig. 4a) may be found in [41,43], in which the thermal requirements for oxygen production are described, as well as the means and equipment required to achieve such conditions with proper engine control.

This work contemplates the engine full-load point at 3500 rpm with exhaust manifold temperature (T_{exh}) = 1000 °C and oxygen to fuel equivalence ratio (λ) = 1.1 as a point of departure, and thereby, all calculations shown in this manuscript are performed taking into account those conditions. Also, Arnau et al. [43] confirmed the uselessness of variable geometry turbocharger (VGT) GO proposed by Serrano et al. [41], since the engine operating range, covering the engine full-load curve and part-load points for some engine speeds, did not require it for controlling T_{exh}, being enough the back pressure valve for that purpose. Thus, as displayed in Fig. 4b, VGT GO and its corresponding cooler C-2 are removed in this work to improve system packaging. Moreover, as the exhaust gas contains unburnt fuel due to incomplete combustion, an after-treatment system, particularly an oxidation catalyst (OC), is placed at the hot-fluid outlet of the heat exchanger (HE) GN to abate CO and HC engine-out emissions, and increase the exhaust gas purity in terms of CO_2 and its temperature at heat exchanger network (HEN) inlet. In particular, the HEN proposed by Serrano et al. [41] is preserved for all the layouts depicted in this manuscript.

Table 3 shows the main average results comparing the model with first amendments (without VGT GO and with OC) to its previous version (with VGT GO and without OC). To do so, an optimization process was carried out actuating on the start of injection (SOI) to maximize the optimization (Opt.) function defined as the product of effective efficiency and engine brake power. There is no considerable difference between the two cases in engine performance which demonstrates that VGT GO is not necessary. Besides, the OC conversion efficiency was 98%, reducing the HC amount from 2147 ppm to 30 ppm thanks to a temperature around 750 °C at the catalyst inlet.

2.3. Coupling carbon capture (CC) model to oxy-fuel layout

This subsection proposes a CC model based on EOS for VLE calculation built in a Python script, considering how to couple it to

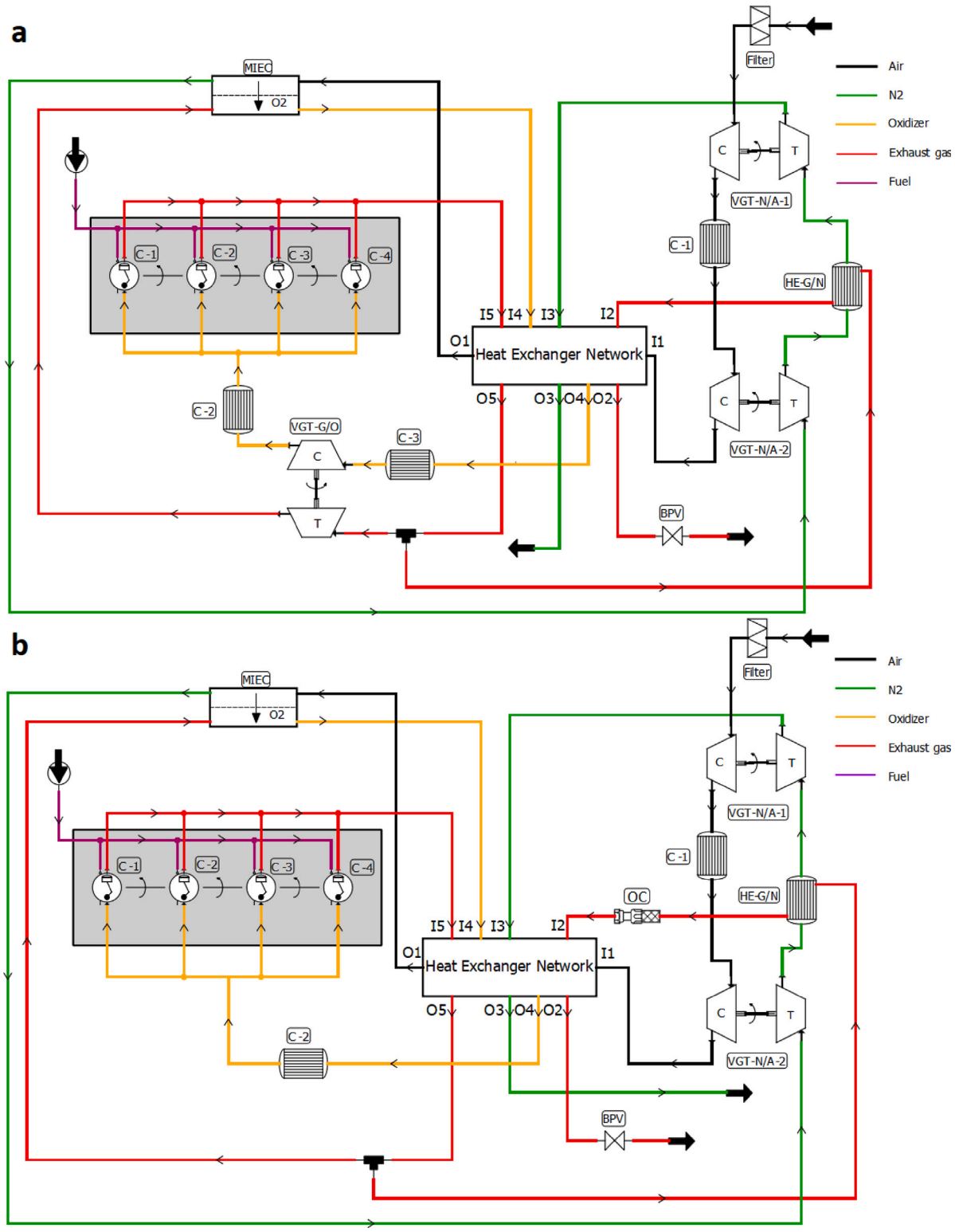

Fig. 4. (a) Original layout established by Serrano et al. [41] and Arnau et al. [43]; (b) Original layout without VGT GO and cooler C-3, and adding an OC.

Table 3
Comparison table for the model with and without VGT GO.

	Brake power [kW]	Effective efficiency [–]	BSFC [g/kWh]	SOI [CAD]	Maximum in-cylinder pressure [bar]	Opt. Function [kW]
VGT GO	111.6	0.337	239.7	−27.4	177	37.68
No VGT GO & OC	111.3	0.338	238.8	−24.6	164	37.71

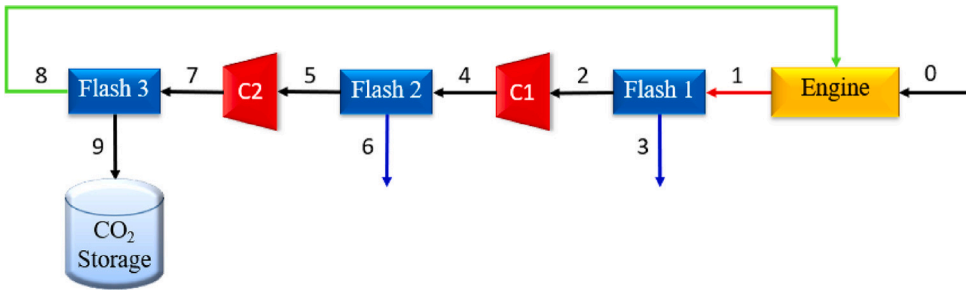

Fig. 5. CC system schematic layout for modeling proposals.

the modified oxy-fuel engine modeled in VEMOD (no VGT GO with OC) and studying the intake cooling effect on system performance. Therefore, parametric studies were performed in order to determine the CC unit operating conditions in terms of temperature, pressure, and composition with the purpose of capturing the CO_2 at near-ambient temperature. In this context, the complete model was established using VEMOD along with a Python script working simultaneously and interdependently, i.e., the VEMOD outputs are the Python script inputs and vice versa.

2.3.1. CC modeling

With the aim of developing a CC model with essential equipment and suitable operating parameters (i.e., temperature, pressure, and composition), average temperature and pressure of the system-out exhaust gas upstream the back pressure valve (BPV) found for the modified oxy-fuel layout (described in Section 2.2) are imposed and held constant as inlet conditions for the CC system at point 1 in Fig. 5. Therefore, the CC system basically consists of two compression steps, three cooling processes with water removal, and a CO_2 storage tank as shown in Fig. 5. Furthermore, only the mass balance with reaction is employed in this work step for the element engine, and oxygen mass flow generated by the membrane found in that last layout configuration is imposed at point 0, assuming the CC system operates regardless of the Brayton cycle. Thus, heat transfer and generation , as well as fluid dynamics are not taken into account to design a preliminary CC model and specify its basic features.

Considering a CO_2-O_2 binary system with CO_2 overall mole composition of 88%, which was obtained using the system-out exhaust gas composition assuming water is completely removed, flash 3 operating conditions are fixed analyzing the phase diagram for that system at 20 °C (Fig. 6). Indeed, CO_2 may be captured without high cooling energy requirements at that ambient temperature. As shown in Fig. 1b, if that binary system has an 88% CO_2 mole composition, no matter the pressure, there is no phase change and, thereby, CO_2 may not be purified from oxygen at temperatures from approximately 25 °C upward. Thus, fixing 20 °C for flash 3, 80 bar seems to be a pressure high enough to liquefy around one-third of overall mole flow, with a reasonable CO_2 purity (around 93% mole composition = 95% mass composition) as displayed in Fig. 6, where y, z, and x represent vapor, overall and liquid CO_2 mole composition respectively, and red and blue horizontal bars denote vapor and liquid mole fraction portions respectively. Indeed, on the one hand, lower pressures would generate more surplus vapor, which must be recirculated to the engine in order to avoid CO_2 emissions. Consequently, more mass flow would be recirculated through the compressors, increasing the energy required by the compression process. On the other hand, higher pressures would decrease captured CO_2 purity.

The 180 L CO_2 tank volume was estimated considering complete combustion of the fuel (n-heptane), and assuming fuel and CO_2 densities at normal conditions and, 20 °C and 80 bar, respectively. Thus, taking into account those densities and supposing a fuel tank capacity of 50 liter (a conventional value for automotive applications), the CO_2 tank volume must be approximately three times higher than the fuel one in order to assure all CO_2 produced by the combustion may be stored when all fuel in the tank is completely consumed. The compressors were calculated as reciprocating compressors assuming 85% isothermal efficiency with the same pressure ratio (around 7) so as to minimize the total compression work to pressurize the CO_2 from 1.65 bar (suction pressure at system-out exhaust gas) to 80 bar in two compression stages. Reciprocating compressors were considered due to their capacity to generate high-discharge pressures compared to other compressors without the need for numerous compression stages [57]. The flash model was defined as a cooling step through a heat exchanger wherein the liquid generated during this process is separated from the vapor phase. As already mentioned in the previous subsection Section 2.1, all-flash calculations were based on VLE thermodynamic behavior calculated with PR EOS. Thus, liquid water is essentially removed from the exhaust gas through flashes 1 and 2, and liquid CO_2 is captured at point 9 after flash 3.

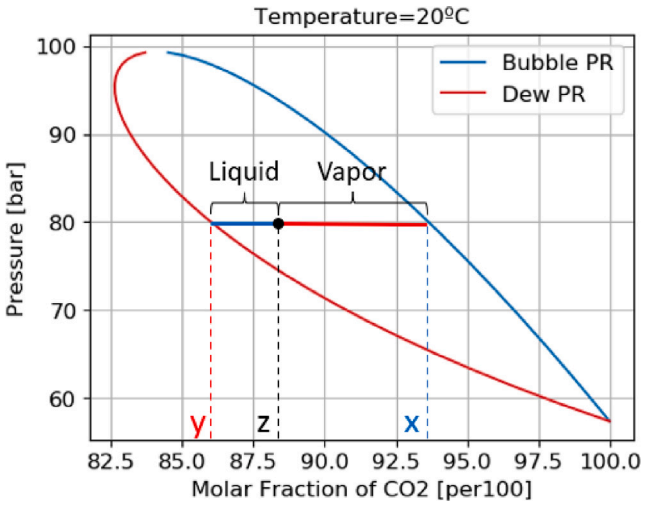

Fig. 6. Phase diagram at 20 °C for the CO_2–O_2 binary system calculated with PR EOS.

Also, the surplus vapor contains a substantial amount of oxygen, which may be considered in the combustion process to provide extra power for the engine. Otherwise, there would be an accumulation of oxygen within the system, and the CO_2 overall mole fraction would move gradually leftwards in Fig. 6, reducing little by little the amount of CO_2 captured in the liquid phase. In addition, as the reciprocating compressors are coupled to the engine, the extra power delivered by combustion may be useful to move the compressors. Therefore, all oxygen (from points 8 and 0) entering the element engine in Fig. 5 is employed in the combustion, keeping the oxygen-to-fuel ratio of 1.1. The injected fuel to achieve that value was computed as expressed in Eq. (12), where st refers to the stoichiometric conditions, $\dot{m}_{fuel}$ and $\dot{m}_{O_2}$ represent the mass flows of fuel and oxygen respectively. In this case,

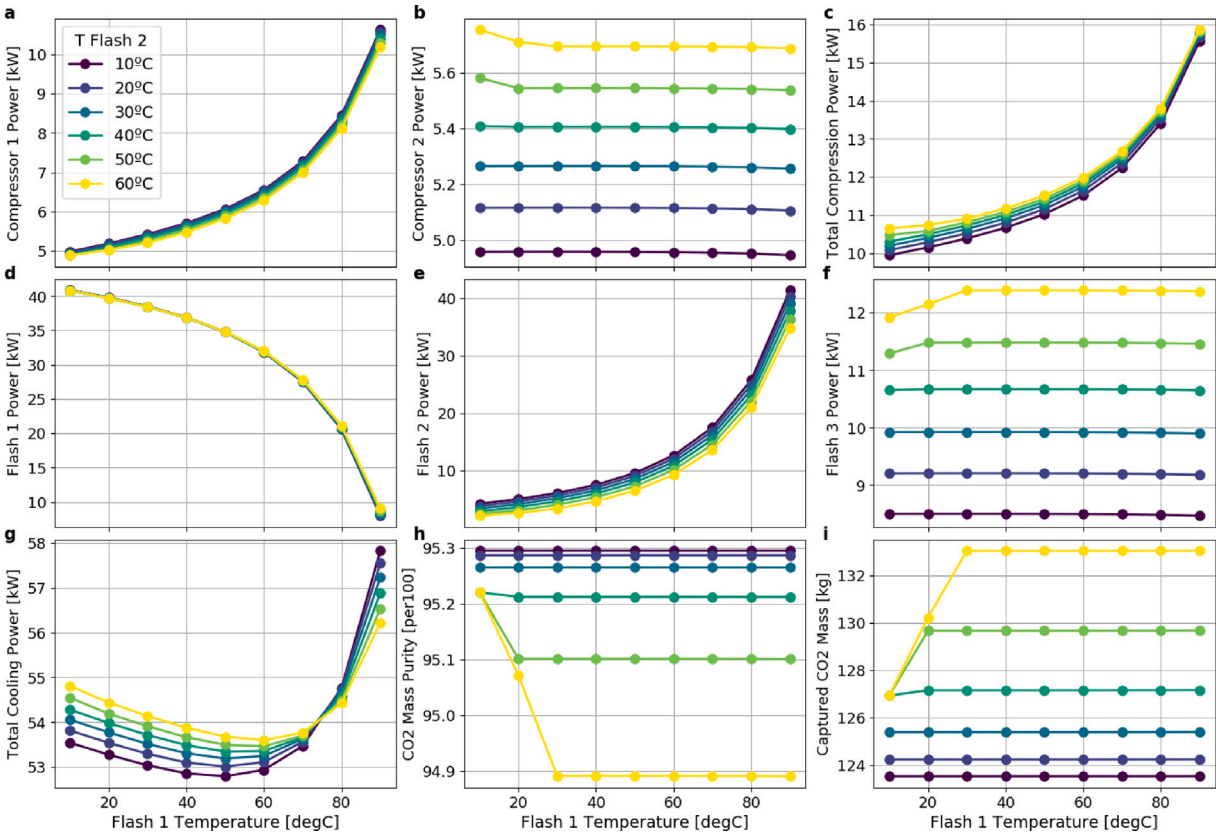

Fig. 7. The main results of the CO_2 capture system performance sweeping flashes 1 and 2 outlet temperatures.

attention should be let to the fact that $\dot{m}_{O_2,0}$ and $\dot{m}_{O_2,8}$ mean oxygen produced by the membrane and recirculated from flash 3 (the product of mass flow and oxygen mass fraction), respectively.

$$\lambda = \frac{\dfrac{\dot{m}_{O_2,0} + \dot{m}_{O_2,8}}{\dot{m}_{fuel}}}{\left(\dfrac{\dot{m}_{O_2}}{\dot{m}_{fuel}}\right)_{st}} \tag{12}$$

With the aim of defining flash 1 and flash 2 outlet temperatures (TF1 and TF2, respectively) and verifying their effects on the CC system performance as operating parameters, a parametric study was carried out varying those variables from 10 °C to 90 °C, and from 10 °C to 60 °C for flashes 1 and 2 respectively (Fig. 7). The flash 2 outlet temperature intends to remove the remaining water (from the flash 1 vapor outlet), purify and dry the CO_2, and decrease the compressor 2 inlet temperature to avoid damaging the compressor and prevent very high temperatures at the Flash 3 inlet. As shown in Fig. 7a, compressor 1 power increases significantly when TF1 is high because of higher compressor inlet temperatures, and less water is condensed in the flash 1, and thereby, more mass flow passes through that compressor. Besides that, compressor 2 is more dependent on TF2 (Fig. 7b) but with less variation when compared to compressor 1 due to lower water content at its inlet, which entails more dependency on the total compression power (defined as the sum of the compressor 1 and compressor 2 powers) on TF1 (Fig. 7c). Flash 1 and flash 2 powers are essentially relying on TF1 (Fig. 7d and e) and, thereby, when TF1 rises, flash 1 power is reduced due to less condensation in this stage, also provoking an increase in mass flow passing through flash 2 and, consequently, raising its cooling power. Thus, since flash 3 power varies slightly with respect to TF2 and it is TF1-independent, the total cooling power (defined as the sum of flash 1, flash 2, and flash 3 powers) presents a minimum value within a narrow TF1 range (approximately from 50 °C to 60 °C) for each TF2 (Fig. 7f and g).

The amount of CO_2 captured, as well as its purity, basically relies on TF2 (Fig. 7h and i) because whenever there is phase change at flash 2, its outlet temperature controls water content at flash 3 inlet since water saturation pressure is fundamentally temperature-dependent. Hence, if TF2 rises, less liquid water is condensed at flash 2, increasing the mass flow entering flash 3 with more water content, which boosts CO_2 liquefaction at flash 3 (Fig. 7i) and increases its cooling power (Fig. 7f), reducing CO_2 purity (Fig. 7h) due essentially to water presence at liquid phase. Nevertheless, there is no condensation in flash 2 at low TF1 (approximately from 10 °C to 30 °C) and high TF2 (approximately from 40 °C to 60 °C), because water vapor pressure is lower than water saturation pressure at TF2 in this case. Thus, the amount of CO_2 captured and its purity is essentially TF1-dependent under those conditions, having an effect equivalent to varying TF2 when there is condensation at flash 2. Finally, authors deem TF1=50 °C and TF2 = 30 °C optimum points to pursue the work presented in this manuscript. In fact, the higher the TF2, the worse the total energy consumption as seen in Fig. 7c and g. However, as temperatures lower than 30 °C could be challenging to achieve due to utility structural limitations using refrigerant fluid or water, that value was set to TF2. Moreover, TF1=50 °C yields a minimum total cooling power at TF2 = 30 °C (Fig. 7g) without substantial penalty in total compression power (Fig. 7c).

2.3.2. *Inner cylinder vapor injection and intake cooling effect*

After having designed the CC system and defined its process variables, the next step consisted of determining the best way to recirculate the flash-3-out vapor to the engine, coupling the CC model to the complete oxy-fuel combustion layout with oxygen generation. Towards that end, the CC model replaced the BPV in the modified oxy-fuel combustion layout (no VGT GO with OC described in Section 2.2) and, thereby, the system-out exhaust gas properties were the inputs at point 1 in Fig. 5. The exhaust manifold gas temperature was maintained at its

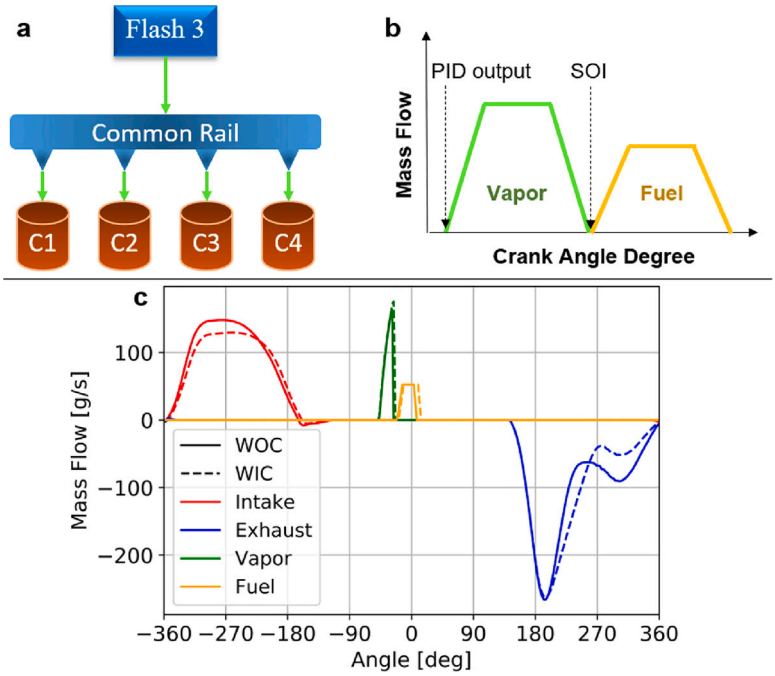

Fig. 8. Common rail for injecting vapor from flash 3 directly into cylinders. (a) Scheme; (b) Pressure control system; (c) Instantaneous inbound and outbound mass flows inside a cylinder for the best SOI of each proposed configuration (WIC and WOC).

set value (1000 °C), employing the pressure imposed on the compressor 1 inlet, which controls the EGR rate and the oxygen dilution level. Also, a common rail was proposed to receive the vapor coming from flash 3 and re-inject it directly inside the cylinders in order to take advantage of its high pressure (80 bar) and low temperature (20 °C), increasing engine volumetric efficiency and hence the in-cylinder trapped mass (Fig. 8a). To do so, a proportional–integral–derivative controller (PID) was used to keep the vapor common rail pressure at 80 bar actuating on the start of vapor injection whose value is the same for all cylinders (Fig. 8b).

Moreover, the end of injection was fixed equal to SOI to ensure all oxygen contained in the vapor was available to react with the fuel. In this way, the discharge pressure (in-cylinder instantaneous pressure) is not very low, which enables to recover part of vapor momentum and pressure through vapor expansion. Also, the amount of vapor injected was uniform throughout the cylinders guaranteeing no mass accumulation inside the vapor common rail, which had a volume equal to 2.0 L to avoid huge pressure fluctuations and PID instability.

Fig. 9 presents the oxy-fuel combustion layout coupled to the CC system with surplus vapor recirculation comparing two cases: with and without a cooler (WIC and WOC, respectively) before the intake manifold. The cooler C-2 model was established by maintaining a cylinder intake temperature of 85 °C to avoid in-cylinder water condensation. The idea is to assess the impact of a cooling step at the cylinder inlet on engine performance and verify if C-2 is not really advantageous and may be removed, facilitating the system packaging.

As the CO_2 reciprocating compressors were connected to the engine crankshaft, part of the mechanical energy produced by combustion was used to move those compressors, and, hence, both engine brake power and BSFC must consider that reduction of available mechanical energy. As a result, net brake power is defined as engine brake power minus the power of the reciprocating compressors, and engine net BSFC is established as the amount of injected fuel by the engine cycle divided by net mechanical energy generated within the same engine cycle. In this circumstance, the net optimization function, defined as the product of net effective efficiency (equivalent to engine net BSFC) and net brake power, was maximized actuating on SOI for the proposed cases (WIC and WOC), whose average results of relevant engine performance variables are compared in Tables 4 and 5. WOC presents higher in-cylinder maximum pressure than WIC because more EGR is required to control T_{exh} at the set point due to the lack of intake cooling. Within this context, once the total ICE additional cooling is defined as the sum of cooler C-1, flash 1, flash 2, and flash 3 powers (plus cooler C-2 power for WIC), WOC requires lower cooling energy than WIC. However, WIC shows higher gross break power than WOC because it needs less EGR, which implies lower MIEC permeate pressure, higher MIEC pressure ratio, and, consequently more oxygen generation to produce heat-released power. As WIC presents a lower intake temperature, engine volumetric efficiency, and gross BSFC are better for that case since it increases inlet flow density and reduces heat losses. Moreover, the net variables follow the same trend as the gross BSFC and brake power due to the reasons mentioned above based on intake temperature. Those assertions are better proven and detailed in Section 3 whereby more process variables (regarding MIEC, HEN, and engine performances) are studied considering the entire system with the final amendments.

One may see that there is an increment in BSFC (around 10%) by comparing both gross and net BSFC values as well as a reduction in brake power (around 9%) due to energy penalty related to the CO_2 capture. Although the net optimization function presents better results for WIC, its cooling energy penalty is not negligible compared to WOC. Indeed, the total ICE additional cooling power for WIC is around twice as high as for WOC, suggesting the best configuration must contemplate an intermediate solution between WIC and WOC. In both cases, the amount of CO_2 captured as well as its purity is the same since flash temperatures are fixed and, as already seen in Fig. 7, those variables basically depend on the CC system specifications.

Fig. 8c depicts the inbound and outbound mass flows inside one of the cylinders for both cases, WIC and WOC. Therefore, it may be seen how the vapor injection controller is operating satisfactorily without overlapping fuel injection, and vapor injection is very narrow with a significant peak due to the high-pressure difference between common rail (80 bar) and combustion chamber during the compression phase (around 15 bar). The effects of vapor in-chamber direct injection on the in-cylinder instantaneous variables (pressure, temperature, and trapped mass) are appropriately presented and discussed in Section 3.

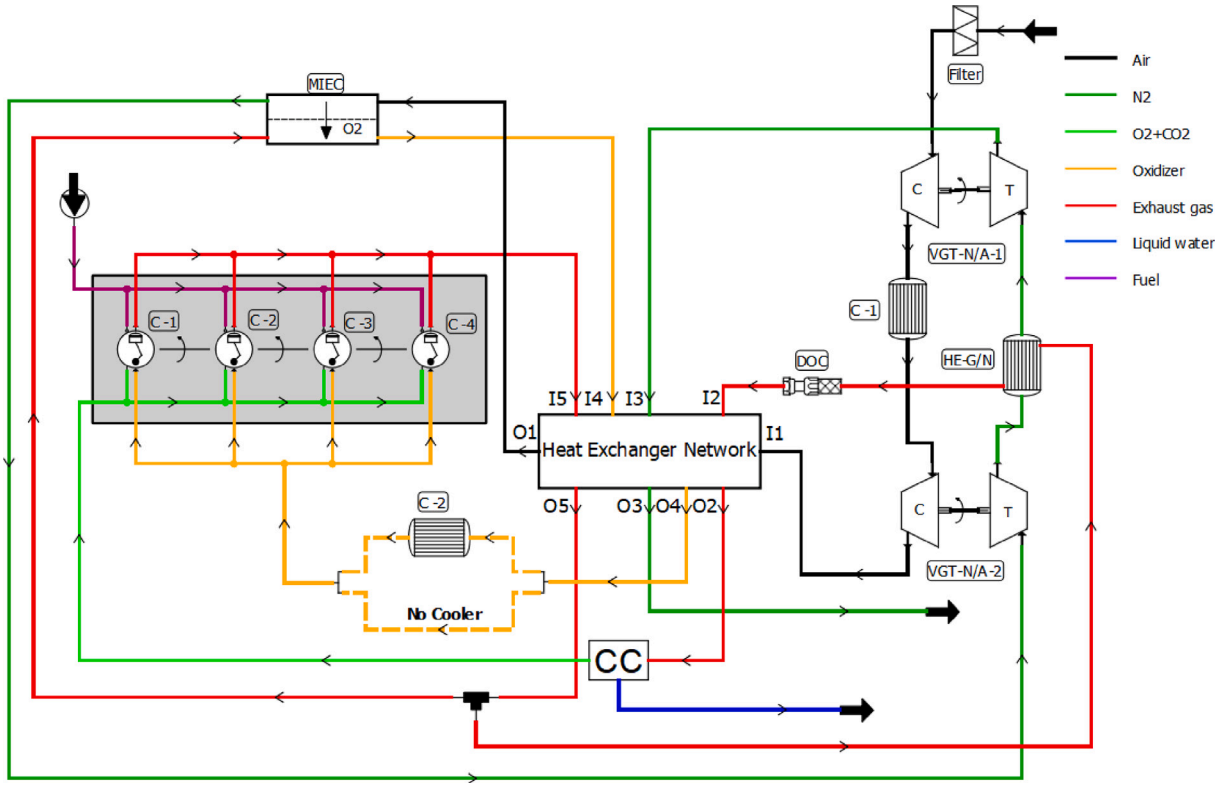

Fig. 9. Oxy-fuel combustion layout coupled to CO_2 capture system with vapor recirculation.

Table 4
Average results of relevant engine performance variables comparing WIC and WOC for the oxy-fuel combustion layout with CC: Part 1.

	BSFC [g/kWh]	Brake Power [kW]	Opt. Function [kW]	SOI [CAD]	Maximum In-cylinder Pressure [bar]	MIEC Permeate Pressure [bar]
WIC	240.3	118.0	39.7	−25.7	164	1.55
WOC	256.4	92.7	29.2	−28.7	180	2.67

Table 5
Average results of relevant engine performance variables comparing WIC and WOC for the oxy-fuel combustion layout with CC: Part 2.

	Net BSFC [g/kWh]	Net Brake Power [kW]	Net Opt. Function [kW]	EGR [%]	Intake Temperature [°C]	Total ICE Additional Cooling Power [kW]
WIC	264.7	107.2	32.7	70.3	85	109
WOC	278.9	85.2	24.7	76.4	374	60

2.4. Water recirculation

In order to take advantage of the main benefits of each solution, i.e., WIC with higher net optimization function and WOC with lower total ICE additional cooling power, a new amendment was proposed. It consisted of recovering part of the liquid water generated by flashes 1 and 2 and blending it with the oxidizer flow to decrease the intake manifold temperature and increase the γ of the intake gas. In fact, as water has greater γ than CO_2 [24], that strategy may be favorable in terms of engine-indicated efficiency. To do so, a pump was added to the CC system to recuperate part of the water leaving flash 1, increasing its pressure until the flash 2 operating pressure Fig. 10. Therefore, liquids from flashes 1 and 2 were mixed and recirculated towards engine intake gases. Fig. 11 displays the proposed layout with a desuperheater (named mixer on the diagram) used to blend water from the CC system with oxidizer flow from HEN.

Regarding the complete model, VEMOD was modeling the vapor injection from the common rail into the cylinders as described in Section 2.3.2, while the Python script was simulating in steady-state the water-oxidizer mixer and the CC system comprising compressors 1 and 2, and flashes 1, 2 and 3. The flow conditions at the oxidizer line (HEN output 4 in Fig. 11) and oxy-fuel layout tailpipe (HEN output 2 in Fig. 11) are the Python script inputs. Indeed, as the EOS-based VLE calculation in different elements of the CC system and mixer is very time-consuming regarding the fluid dynamic as done in VEMOD, the Python script was only activated during certain periods considering the input average values generated by VEMOD. Thus, the Python script outputs were returned to the VEMOD-built oxy-fuel layout as inputs (surplus vapor and water recirculations) in an iterative process between VEMOD and Python script until the system could converge.

2.4.1. Mixer model

Consequently, a mixer model was developed regarding the above context. The mixer outlet may contain either a vapor phase, which means all liquid water is evaporated by the oxidizer flow, or a VLE phase with considerable liquid water content depending on mixer inlet flow conditions. In order to determine the mixer outlet conditions (mass flow, composition, temperature, and phase), the mixer model algorithm solved mass and energy balances coupled to VLE equations, considering the mixer as adiabatic and the inlet liquid water discharge

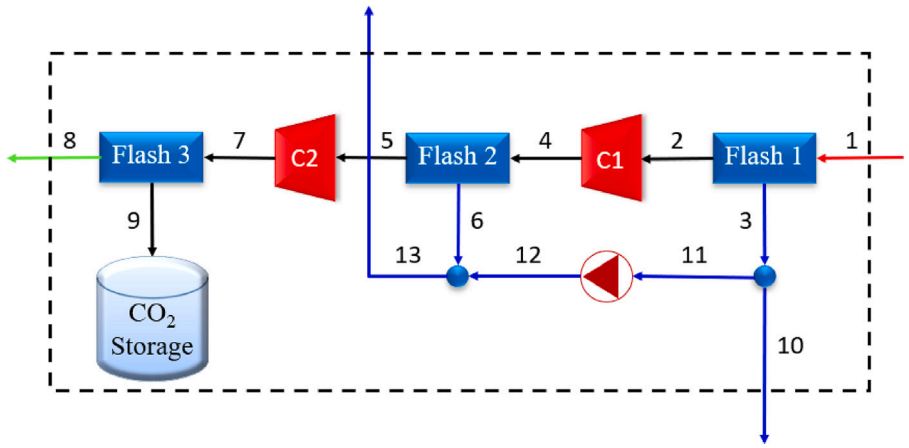

Fig. 10. CC model with water recirculation.

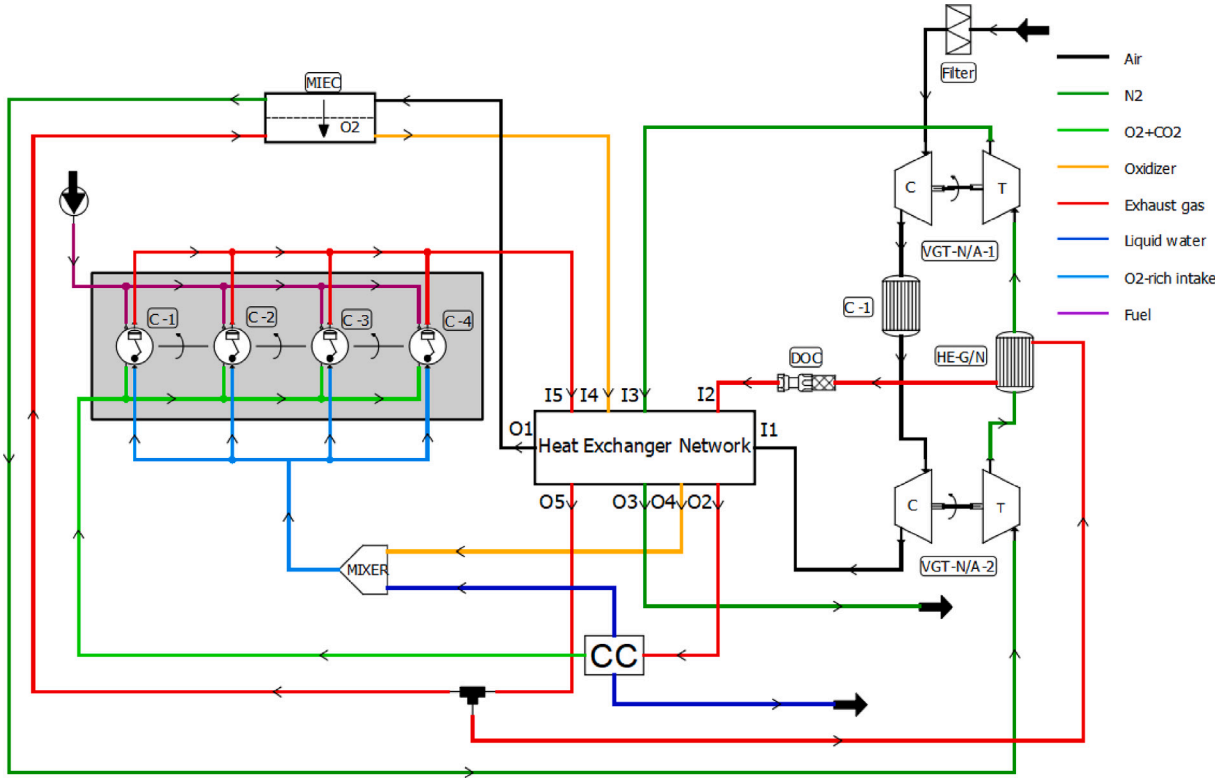

Fig. 11. Oxy-fuel combustion layout coupled to CO_2 capture system with water recirculation.

pressure equal to the inlet oxidizer flow pressure. The mixer outlet phase was verified by comparing the mixture dew enthalpy with the mixture outlet vapor enthalpy, which was calculated assuming the oxidizer has enough thermal energy to evaporate all liquid water and, hence, the mixer outlet phase was assured to be vapor. Both enthalpies were respectively calculated using Eq. (5) with dew-point vapor mole composition and outlet overall mole composition considering the mixer mass balance. In short, if the mixture outlet vapor enthalpy is greater than the mixture dew enthalpy, the outlet phase is a vapor; otherwise, it is a VLE mixture for a given operating pressure.

To demonstrate the mixer model performance, oxidizer conditions (mass flow, composition, temperature, and pressure) were held constant for the point with a better net optimization function for the WOC case. Therefore, a sweeping process varying inlet liquid water temperature (from 30 °C to 90 °C) and mass flow (from 0 $kg\,h^{-1}$ to 150 000 $kg\,h^{-1}$) was carried out by tending to infinite the amount of water injection for the sake of better illustrating the physics of the process.

As shown in Fig. 12b, there are two distinct zones: one where the outlet phase is a vapor corresponding to low water mass flows (WMFs) (approximately from 0 $kg\,h^{-1}$ to 50 $kg\,h^{-1}$), and another where outlet phase is a VLE corresponding to high WMFs (approximately from 50 $kg\,h^{-1}$ to 150 000 $kg\,h^{-1}$). The mixer outlet temperature profoundly decreases when inlet WMF increases within the vapor zone because little-by-little significant latent energy is required to evaporate all liquid water. In contrast, it tends to the respective water inlet temperature when oxidizer mass flow is not comparable to WMF anymore inside the VLE zone (Fig. 12a). Water vapor pressure increases with WMF inside the vapor region because more water content is present in the outlet gas until achieving saturation condition and, consequently, the VLE zone (Fig. 12c). Indeed, that saturation point corresponds to a stable temperature area (around 100 °C in Fig. 12a), wherein water

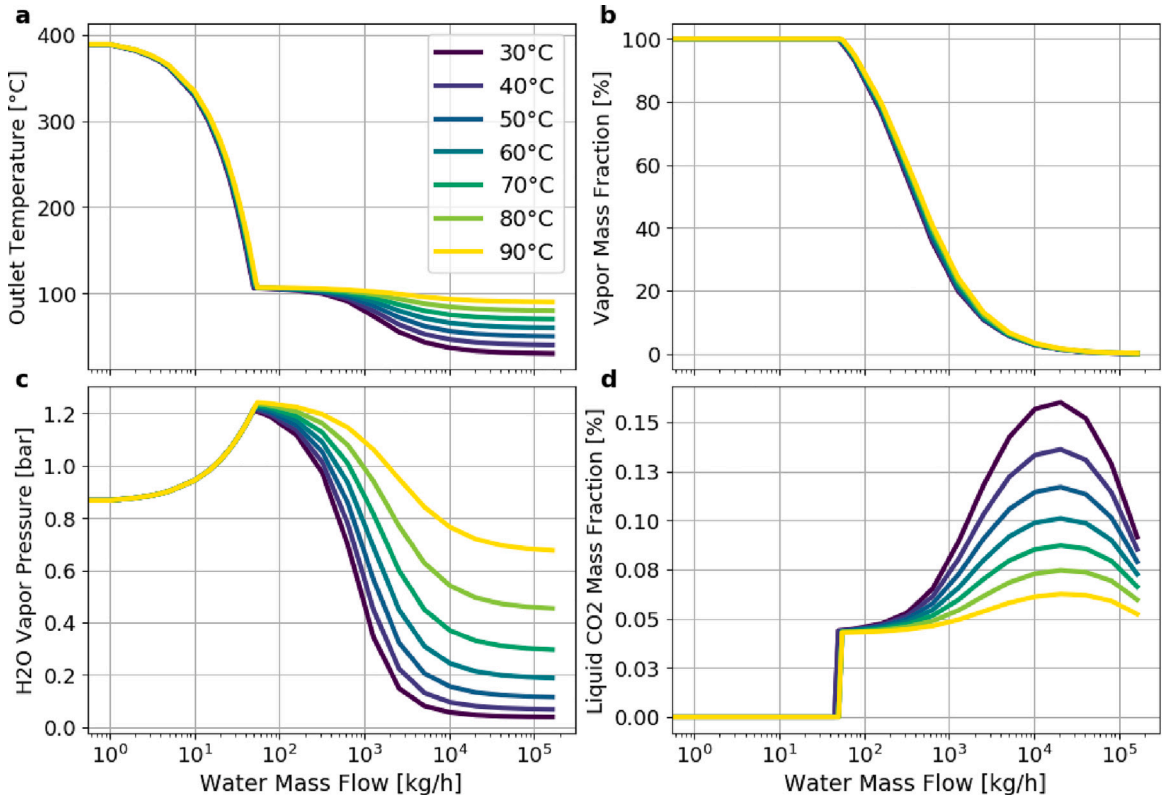

Fig. 12. Main mixer model outlet variables sweeping water temperature and mass flow for given EGR conditions.

pressure vapor is basically equal to its saturation pressure, which is significantly temperature-dependent. Still in Fig. 12c, when WMF is much higher than the oxidizer mass flow, water vapor pressure is WMF-independent because the temperature is essentially equal to the water inlet temperature. The mixer model may predict the solubility of both O_2 and CO_2 in liquid water, which is illustrated in Fig. 12d. On the one side, the liquid CO_2 mass fraction is majorly temperature-dependent, analyzing both Fig. 12a and 12d, and the lower temperature is, the higher CO_2 solubility due to lower gas kinetic energy level. On the other side, a water dilution effect is seen when there is a considerable amount of WMF at constant outlet temperature, which reduces CO_2 solubility (after the peak in Fig. 12d). Also, information about CO_2 solubility is important to define the use of that CO_2-contaminated water since CO_2 dissolving into the water may form carbonic acid, which may corrode alloys and steels present in the engine components.

3. Results and discussion

After proposing a complete oxy-fuel combustion layout with CC and vapor and water recirculations (Fig. 11), SOI and WMF are swept to verify their impact on the performance of relevant engine variables attempting to find out the best-operating conditions for the system. In order to avoid liquid water inside the cylinders, this study pursues operation zones wherein the intake temperature is above the dew point at the intake manifold. As a result, saturation conditions limit the increase in recirculated water for a given SOI. Therefore, this section analyzes critical average results to define the system's optimum operating point with insights into the instantaneous results for the cases of interest. In particular, temperature, pressure, and mass flow along the system are discussed for the best cases without and with water. Finally, an overall analysis of the final results is made Section 3.4.

3.1. Average results

Figs. 13 and 14 present relevant average results in contour maps varying SOI and total ICE additional cooling power, which is basically WMF-dependent (the amount of recirculated water is represented by white lines drawn over maps). As expected, the higher the WMF, the lower the intake temperature (Fig. 13a). Also, if SOI is delayed for a specific WMF, more thermal energy is available at the exhaust manifold and, hence, more EGR is required to control the target temperature (Fig. 13b), heating up the oxidizer flow. Indeed, to produce more EGR, the intake pressure must be increased (Fig. 13c), which entails more intake mass flow (Fig. 13d). The in-cylinder maximum pressure is essentially SOI-dependent (Fig. 13e) and its value decreases when SOI is delayed because the combustion is moved towards the expansion process. Actually, MIEC oxygen generation increases with recirculated water (Fig. 14a) due to the MIEC permeate pressure reduction (following the EGR and intake pressure behaviors) (Fig. 14b), reflecting on an enhancement of the MIEC pressure ratio (Fig. 14c), since MIEC feed pressures scarcely vary (Fig. 14d). Thus, it improves the MIEC filtration efficiency defined by the ratio between the O_2 produced and the total O_2 which enters the MIEC feed side (Fig. 14e). Additionally, the oxygen permeated by the MIEC increases due to higher MIEC feed temperature (Fig. 14f) risen by the higher exhaust gas thermal power with greater water content. As a result, the increment of in-cylinder available oxygen produces more energy released by combustion and, consequently, more mechanical power (Fig. 13h) and cylinder-out gas sensible enthalpy to heat up the MIEC. Also, as water-specific heat capacity is greater than that of CO_2, if more water is recirculated, the better the efficiency in many HEs. In other words, once this system is self-sufficient, the more oxygen generated by the MIEC, the better the system works, increasing its oxygen production rate.

Fig. 13f shows minimum values for system-inlet air mass flow when the WMF varies at a constant SOI, which is also observed on the

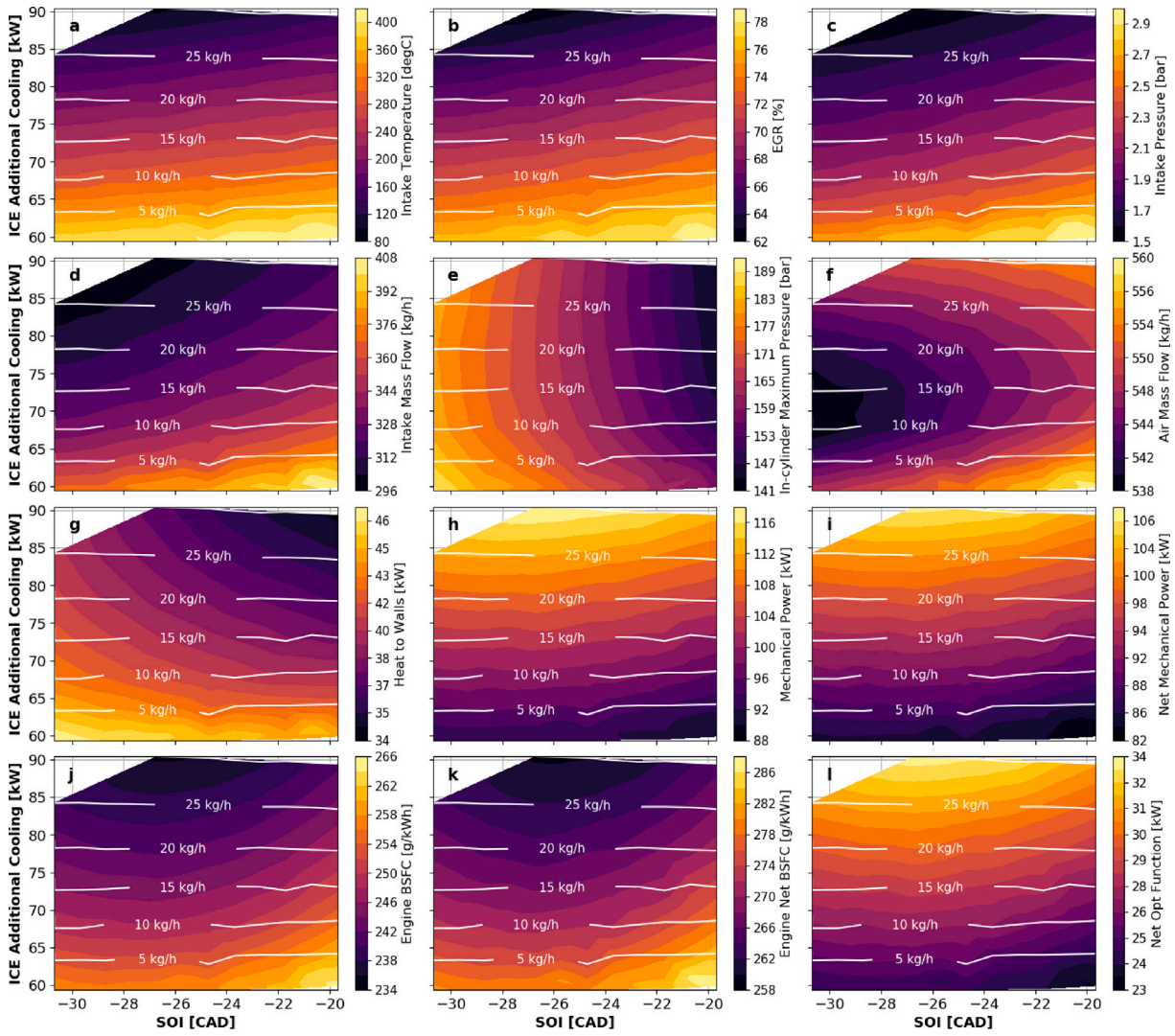

Fig. 13. Maps for average results of relevant engine variables sweeping SOI and total ICE additional cooling power (reflected by the amount of water blended with EGR at mixer). The white lines drawn on maps represent the amount of recirculated water.

MIEC feed pressure (Fig. 14d). On the one hand, if the MIEC filtration efficiency is improved, less mass flow is present at the N_2-rich line and less energy is available to move N_2 turbines of VGT NA-1 and VGT NA-2 (bottom part over Fig. 13f with WMF range from $0\,kg\,h^{-1}$ to $15\,kg\,h^{-1}$). On the other hand, when O_2 production is high, more exhaust mass flow is generated leading to more heat power exchanged at the HEs, producing more thermal power to move the N_2 turbines (Fig. 14d and 14f), which compensates the increase in MIEC filtration efficiency (top part over Fig. 13f with WMF range from $15\,kg\,h^{-1}$ to $30\,kg\,h^{-1}$). In turn, convective heat losses decrease when WMF increases due to the intake cooling effect (Fig. 13a and g), and at constant WMF, if SOI is delayed, more intake fresh mass flow with more inert is sucked by the engine, reducing the heat transfer to walls due to the presence of more mass that absorbs the heat released by the combustion (Fig. 13b and d). The main advantage of using recirculated water is reflected in the improvement of the system performance variables such as engine power, net engine power, BSFC, net BSFC, and net optimization function (Fig. 13h-l). In fact, as more oxygen is produced and less convective heat is wasted when the WMF increases, more useful energy is available to yield worthwhile mechanical power with better efficiency since the gamma of the cylinder oxidizer charge is also higher. In general, the penalty for capturing CO_2 in-situ (moving the reciprocating compressors coupled to the engine) is seen in the reduction of mechanical power (around 8%) and the increase in BSCF (around 9%), comparing Fig. 13h and i as well as Fig. 13j and k, respectively. Fig. 13l depicts a trade-off between the cost of chilling and system performance since improvement on net optimization function entails higher total ICE additional cooling power. Therefore, the authors consider WMF = $20\,kg\,h^{-1}$ and SOI=-26.5 CAD the preferred point without excessive cooling power and with satisfactory engine output.

3.2. Instantaneous results

Fig. 15 displays instantaneous results of in-cylinder variables for the edges of the contour maps (blue and green lines) and the chosen combination of SOI and WMF, taking into account the trade-off between total ICE additional cooling power and net optimization function (red line). Green and blue lines represent the most advanced and delayed SOIs, respectively, whereas solid and dashed lines represent the highest and lowest WMFs for each specific SOI. One may see that when the combustion is more centered at the top dead center (Fig. 15a and c), the effective efficiency is improved (Fig. 13j and k). The effect of in-cylinder direct vapor injection is observed in Fig. 15b and d, with a slight increment of in-cylinder oxygen mass, decreasing the temperature during the compression phase. Still within that phase, the cases without water recirculation present higher pressure (Fig. 15c) due to more EGR need (Fig. 13b) to keep exhaust gas temperature of 1000 °C, also reflecting on more elevated maximum pressure (Fig. 13e).

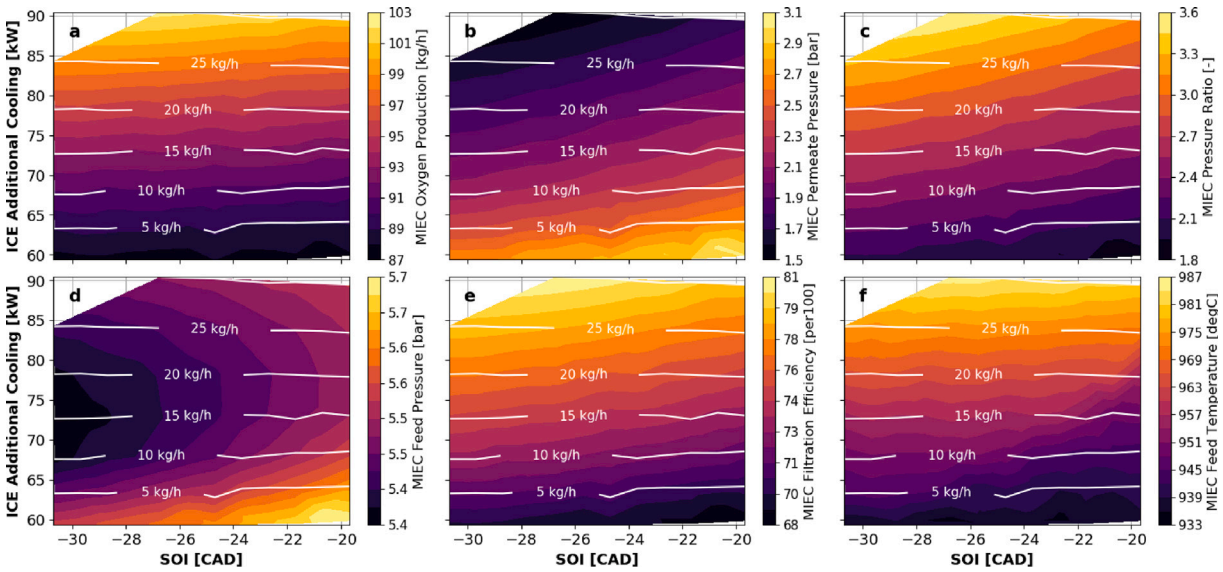

Fig. 14. Maps for average results of relevant MIEC variables sweeping SOI and total ICE additional cooling power (reflected by the amount of water blended with EGR at mixer). The white lines drawn on maps represent the amount of recirculated water.

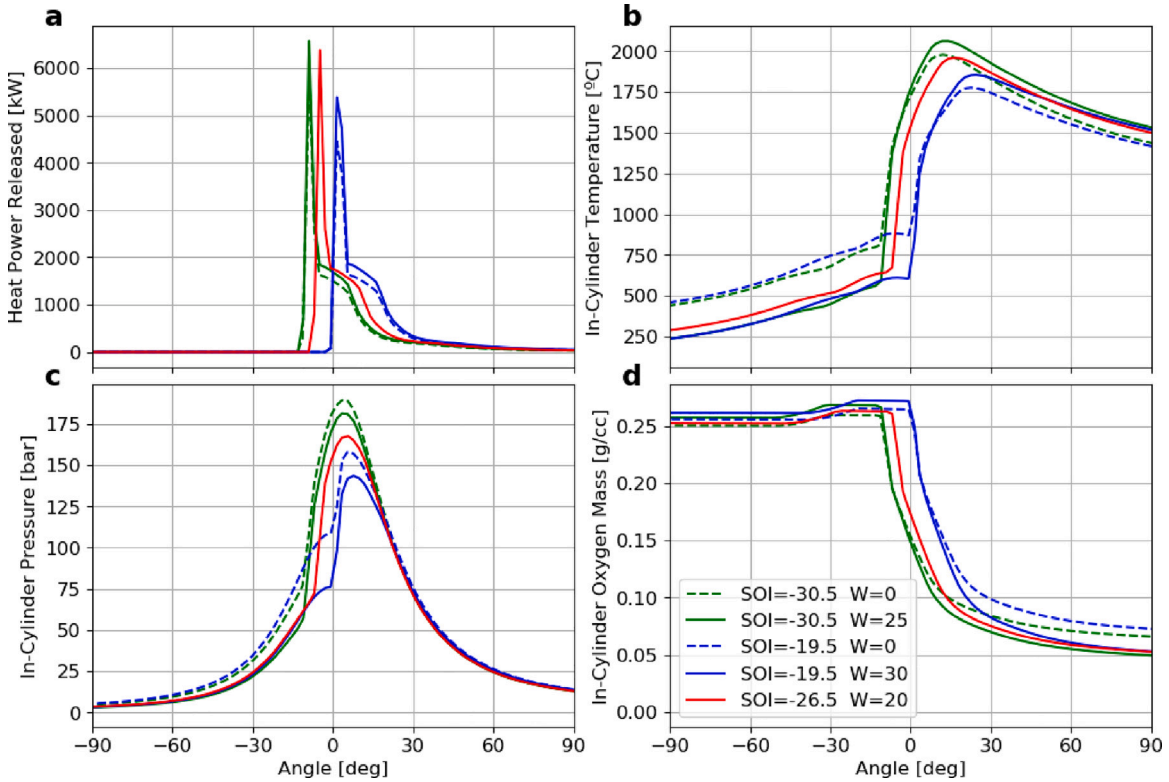

Fig. 15. Instantaneous results of in-cylinder parameters for the edges of the contour maps and the chosen combination of SOI and amount of recirculated water, taking into account the trade-off between total ICE additional cooling power and net optimization function. In the figure legend, SOI is in CAD and W represents the water recirculated in kg/h.

In addition, once more oxygen is employed for cases with water recirculation, more heat power is released during combustion (Fig. 15a), generating more brake power (Fig. 13h and i).

3.3. Temperature, mass flow, and pressure diagrams

This subsection analyzes the preferred point (in terms of total ICE additional cooling power and net optimization function) for each case with and without water recirculation (WIR and WOR, respectively) by checking the process variables drawn over distribution diagrams (Figs. 16 and 17):

- WMF = 20 kg h^{-1} and SOI = −26.5 CAD for WIR.
- WMF = 0 kg h^{-1} and SOI = −27.5 CAD for WOR.

Fig. 16 displays powers and temperatures on different lines and elements of the system, including the HEN. Numerical values are added next to each flow line with top values for WIR and bottom ones for

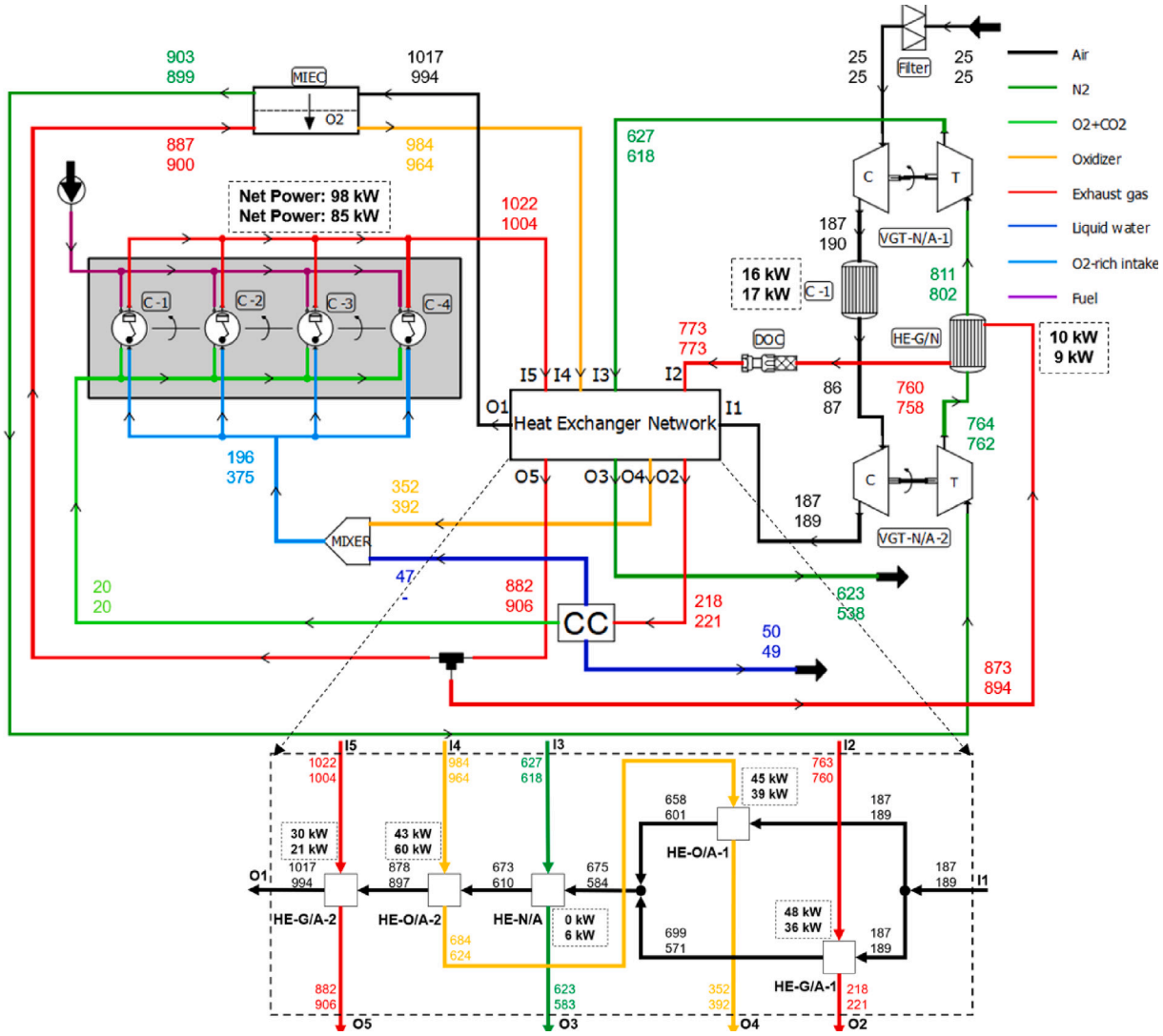

Fig. 16. Power (in kW) and temperature (in °C) distribution diagram for both cases at 3500 rpm: with (top values) and without (bottom values) water recirculation.

WOR. In addition, the heat power exchanged is shown next to each HE and cooler, as well as the net system power over the engine itself, following the representation mentioned above. Also, Fig. 17 shows the effect of each case on mass flow and pressure distributions, following the same depiction scheme as for the temperature diagram (with top values for WIR and bottom ones for WOR). Indeed, those diagrams confirm the analyses carried out for contour maps (Figs. 13 and 14), demonstrating the benefits of water recirculation on system performance (see Net BSFC and Net Power on Figs. 17a and 16, respectively). Compared to WIR, WOR has higher pressure at MIEC permeate side with more EGR mass flow to maintain T_{exh}=1000 °C, and, thereby, less oxygen is generated by the MIEC since its feed pressure is almost constant. However, less EGR is required to control that temperature when there is water recirculation, which improves the pressure ratio at the MIEC and its O_2 production. If more O_2 is available for combustion, the engine power output increases, and more mechanical power is free to move the reciprocating compressors in the CC. Once λ is fixed in both cases, more fuel is also injected when more oxygen permeates the MIEC, thereby generating more combustion products (CO_2 and water vapor). Thus, that increment of mass flow going towards CC, also due to water recirculation, causes more heat transfer in the HE GA-1, and, hence, changes the power distribution through the HEs. In addition, as the specific heat capacity for water is almost double that for CO_2 [24], the heat transfer is improved in a particular HE when there is more water content on any of its sides. Also, the intake manifold water content increases from 18% to 27%, enhancing the in-cylinder γ and, hence, the engine indicated efficiency.

Nonetheless, as WIR possesses more water vapor at exhaust gas going towards CC, Flash 1 cooling power must be higher because TF1 is the same for both cases, which increases the total ICE additional cooling power as explained in Section 2.3.1. In any case, the heat exchanged in the Flash 1 is much higher than for Flashes 2 and 3 due to their outlet temperatures, which are defined in Section 2.3.1. Whenever there is water recirculation, the pump shown in Fig. 10 is required; however, once the liquid density is much higher than for gases, its pumping power (around 0.005 kW) is negligible compared to the gas compression power on reciprocating compressors (around 7 kW and 9 kW for the first and second compression stages respectively). As more CO_2 is produced for the WIR case than for WOR one, its corresponding time to consume the fuel (at this particular operating point) and fill up the CO_2 storage tank is shorter (around 93 min and 104 min for WIR and WOR, respectively) to capture the same amount of mass (around 125 kg) at 25 °C and 80 bar with the same CO_2 purity equal to 95% (mass fraction). For additional information about the CC, please see the supplementary material with the distribution diagrams for both configurations following the representation depicted in Figs. 16 and 17.

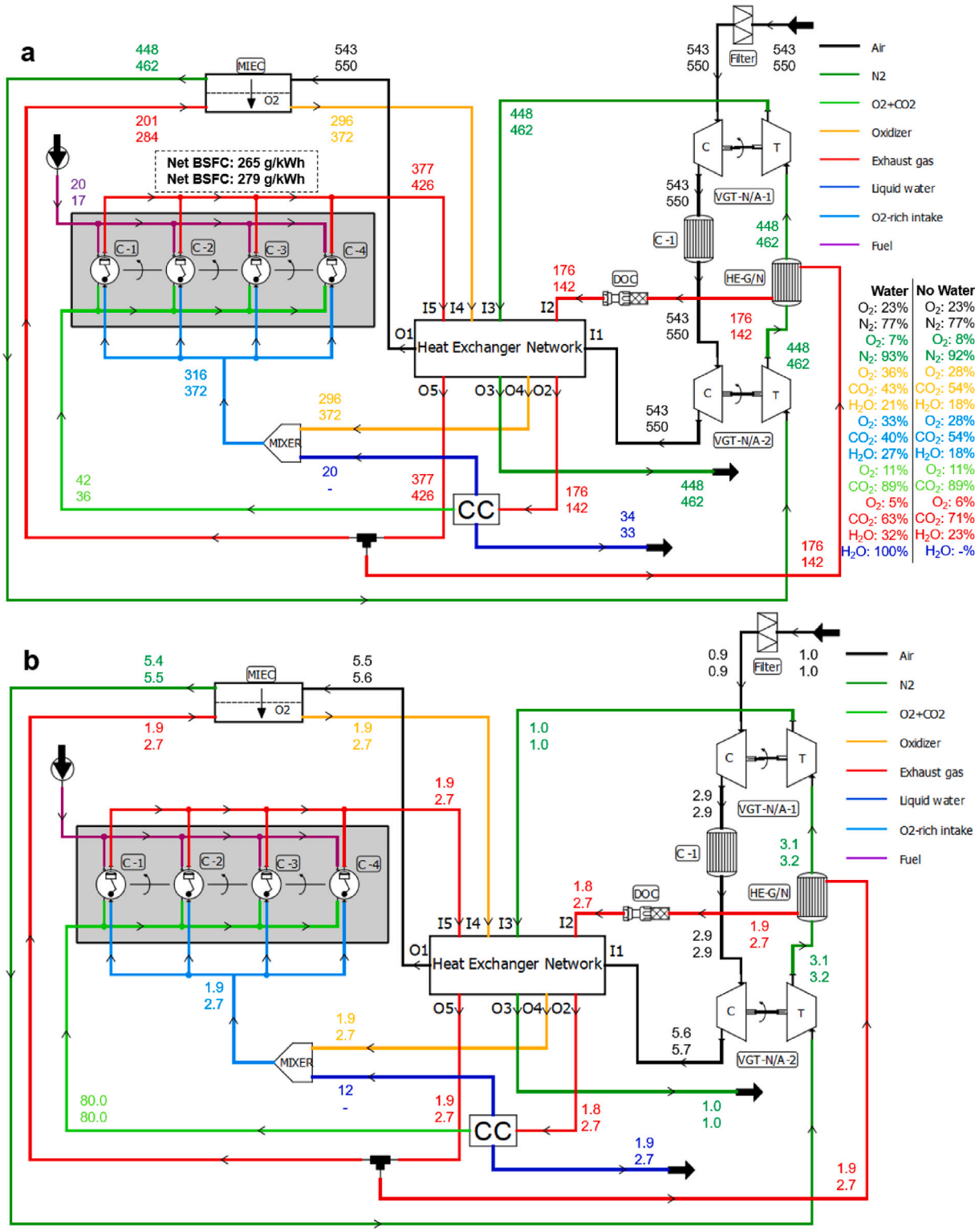

Fig. 17. Distribution diagram for both cases at 3500 rpm: with (top values) and without (bottom values) water recirculation. (a) Mass flow (in $kg\,h^{-1}$) and composition; (b) Pressure (in bar).

As the blow-by flow generated in the cylinders is recirculated into the intake manifold and vapor generated in the Flash 3 is directly re-injected into the combustion chamber, the only losses of CO_2 from the system are related to non-recirculated condensed water on Flash 1 (and Flash 2 for the WOR case), which contains some traces of CO_2 diluted in the liquid phase. Thus, CO_2 capture efficiency may be calculated for the optimum points of the WIR and WOR cases, carrying out a mass balance for the CO_2 considering its mass flows and compositions in the non-recirculated water and CO_2 tank inlet streams. Accordingly, the CO_2 capture efficiencies (or CO_2 recovery rates) calculated for WIR and WOR are 99.94% and 99.87%, respectively using the values presented in the supplementary material.

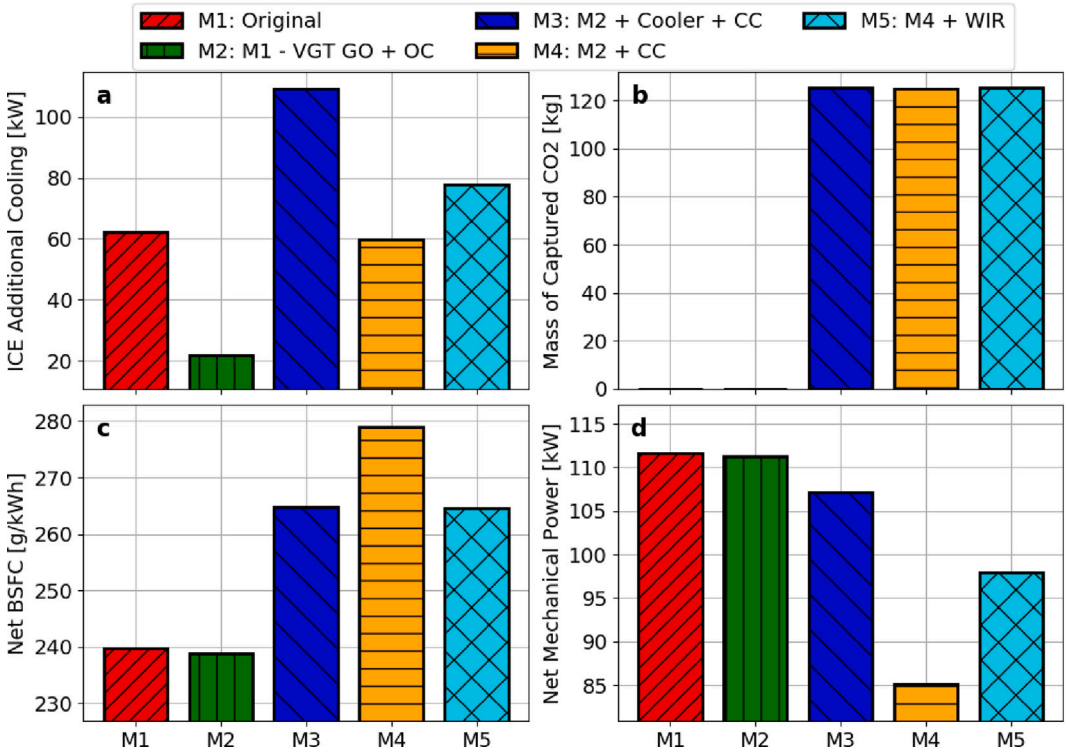

Fig. 18. Overall results for the main amendments.

3.4. Overall results

Fig. 18 summarizes the preferred results of each amendment proposed in this manuscript. In fact, the abbreviation depicted in that figure and used in this subsection represents the following modifications of the layout:

- Original layout established by Arnau et al. [43] (M1).
- Layout M1 without VGT GO and its corresponding cooler, adding an oxidation catalyst (M2).
- Layout M2 with a cooler upstream of the intake manifold and the coupling of the CC system. This configuration is equivalent to the WIC case shown in Section 2.3.1 (M3).
- Layout M2 with the coupling of the CC system. This structure is equivalent to WOC and WOR cases seen, respectively, in Sections 2.3.1 and 3.3 (M4).
- Layout M4 with water recirculation. This configuration represents the WIR case in Section 3.3 (M5).

The results shown for M1, M2, M3, and M4 consider the preferred SOI only with regard to net optimum function, while M5 takes into account that variable combined with the total ICE additional cooling power as explained in Section 3.1. In general, a worsening of the engine performance (higher net BSCF and lower net mechanical power) is seen (Fig. 18c and d) due to the system capability of capturing the CO_2 present in the exhaust gas (Fig. 18b). As already discussed in Section 2.2, M1 and M2 have similar performance, a part of M2 presenting lower ICE additional cooling energy because the cooler upstream the VGT GO is also removed in this case (Fig. 18a). M5 is able to combine the advantages of M3 and M4 when the CC is deemed with in-cylinder direct injection of the surplus vapor coming from flash 3. Thus, M5 yields the same net BSFC as M3, with a slight reduction in net mechanical power, but decreasing considerably total ICE additional cooling power (approximately from 110 kW to 80 kW). In addition, although M5 presents more cooling energy than M4, an important improvement in engine efficiency and output power is observed for M5 (on average, more than 5% and 13% respectively), which confirms M5 as the best layout discussed in this work.

4. Conclusions

An oxy-fuel combustion engine concept with in-situ O_2 separation and CC is studied through several amendments to a layout proposed in the literature. Indeed, the oxy-fuel combustion applied to power plants enables to capture CO_2 in the liquid phase by means of inter-cooling compression stages with water removal, and in this manuscript, the energy cost of that process is assessed as well as the ways to design and integrate it into the powertrain system. To do so, the PR EOS is calibrated with experimental data found in the literature for each pair of substances and used to predict the VLE behavior in many elements to model the CO_2 purification process properly.

The first layout modification was based on removing VGT GO with its corresponding cooler and adding an oxidation catalyst. Afterward, a CC system, composed of two reciprocating compressors, three flash units, and one CO_2 storage tank, was designed taking into account the flash outlet temperatures and pressures. Thus, the best values found in terms of energy consumption for TF1, TF2, TF3, and flash 3 pressure are 50 °C, 30 °C, 20 °C and 80 bar. Moreover, the surplus vapor leaving flash 3 was directly injected into the cylinders in order to increase the in-cylinder trapped mass and produce extra mechanical power with the excess of oxygen to move the reciprocating compressors. Although a cooler upstream of the intake manifold enhances the engine performance by increasing engine volumetric efficiency and collaborating with O_2 production by decreasing the MIEC permeate side pressure, its cooling power may not be negligible. Consequently, a mixer model was developed to recirculate part of the water condensed in flashes 1 and 2 towards the cylinder inlet to lower intake gas temperature and increase the γ of the oxidizer, improving the engine's effective efficiency. Moreover, a sweeping process was carried out with varying SOI and WMF to find the best engine operating conditions.

After the sweeping process, WMF = 20 kg h^{-1} and SOI=-26.5 CAD was deemed the optimum point, taking into account the trade-off between chilling power and engine performance. In fact, this case merges the main benefits of the approaches WIC and WOC, reducing WIC total ICE additional cooling power from 110 kW to 80 kW and

increasing the WOC net optimization function from 25 kW to 30 kW. Finally, upcoming research will extend the engine operation map range towards other engine speeds and load levels considering the onboard oxygen generation with MIECs and CO_2 capture.

CRediT authorship contribution statement

J.M. Luján: Conceptualization, Supervision, Project administration. **F.J. Arnau:** Supervision, Funding acquisition, Software, Methodology, Writing – review & editing. **P. Piqueras:** Writing – review & editing, Conceptualization, Visualization. **V.H. Farias:** Writing – original draft, Investigation, Methodology, Software, Validation.

Declaration of competing interest

The authors declare the following financial interests/personal relationships which may be considered as potential competing interests: F. H. Farias reports financial support was provided by Government of Valencia.

Data availability

No data was used for the research described in the article

Acknowledgments

This work has been partially supported by Grant PID2021-123351OB-I00 funded by MCIN/AEI/ 10.13039/501100011033 and, as appropriate, by "ERDF A way of making Europe". In addition, the work has been supported by Grant CIPROM/2021/061 funded by Generalitat Valenciana, Spain. Finally, the Ph.D. candidate Vitor Farias has been funded by Generalitat Valenciana, Spain (GRISOLIAP/2020/078).

Appendix A. Supplementary data

Supplementary material related to this article can be found online at https://doi.org/10.1016/j.enconman.2023.116979.

References

[1] Rahimi M. Public awareness: what climate change scientists should consider. Sustainability 2020;12(20). http://dx.doi.org/10.3390/su12208369.
[2] European Commission. An european strategy for low-emission mobility, https://ec.europa.eu/clima/policies/transport_en#tab-0-0.
[3] United States Environmental Protection Agency. Greenhouse gas emissions from a typical passenger vehicle, https://www.epa.gov/greenvehicles/greenhouse-gas-emissions-typical-passenger-vehicle.
[4] Babayev R, Andersson A, Dalmau A, Im H, Johansson B. Computational optimization of a hydrogen direct-injection compression-ignition engine for jet mixing dominated nonpremixed combustion. Int J Engine Res 2021;23(5):754–68. http://dx.doi.org/10.1177/14680874211053556.
[5] Wooldridge MS, Singh R, Gutierrez LG, Clancy S. Survey of strategies to reduce cold-start particulate, CO, NOx,and hydrocarbon emissions from direct-injection spark-ignition engines. Int J Engine Res 2022. http://dx.doi.org/10.1177/14680874211068576.
[6] Dreizler A, Pitsch H, Scherer V, Schulz C, Janicka J. The role of combustion science and technology in low and zero impact energy transformation processes. Appl Energy Combust Sci 2021;7:100040. http://dx.doi.org/10.1016/j.jaecs.2021.100040.
[7] Pastor JV, García-Oliver JM, Micó C, Garcia A. An experimental study with renewable fuels using ECN spray A and D nozzles. Int J Engine Res 2021;146808742110312. http://dx.doi.org/10.1177/14680874211031200.
[8] Buhre B, Elliott L, Sheng C, Gupta R, Wall T. Oxy-fuel combustion technology for coal-fired power generation. Prog Energy Combust Sci 2005;31:283–307. http://dx.doi.org/10.1016/j.pecs.2005.07.001.
[9] Simpson A, Simon A. Second law comparison of oxy-fuel combustion and post-combustion carbon dioxide separation. Energy Convers Manage 2007;48:3034–45. http://dx.doi.org/10.1016/j.enconman.2007.06.047.
[10] Carrasco Maldonado F, Spörl R, Fleiger K, Hoenig V, Maier J, Scheffknecht G. Oxy-fuel combustion technology for cement production - state of the art research and technology development. Int J Greenh Gas Control 2016;45:189–99. http://dx.doi.org/10.1016/j.ijggc.2015.12.014.
[11] Escudero A, Espatolero S, Romeo L. Oxy-combustion power plant integration in an oil refinery to reduce CO_2 emissions. Int J Greenh Gas Control 2016;45:118–29. http://dx.doi.org/10.1016/j.ijggc.2015.12.018.
[12] Wei X, Manovic V, Hanak D. Techno-economic assessment of coal-or biomass-fired oxy-combustion power plants with supercritical carbon dioxide cycle. Energy Convers Manage 2020;221:113143. http://dx.doi.org/10.1016/j.enconman.2020.113143.
[13] Pamminger M, Buyu W, Hall C, Vojtech R, Wallner T. The impact of water injection and exhaust gas recirculation on combustion and emissions in a heavy-duty compression ignition engine operated on diesel and gasoline. Int J Engine Res 2019;21:1555–73. http://dx.doi.org/10.1177/1468087418815290.
[14] Osman A. Feasibility study of a novel combustion cycle involving oxygen and water. SAE technical papers, 2009, p. 14. http://dx.doi.org/10.4271/2009-01-2808.
[15] DieselNet Technology Guide. Engine Emission Control, https://dieselnet.com/tech/engine_emission-control.php.
[16] Li X, Peng Z, Pei Y, Ajmal T, Rana K, Aitouche A, et al. Oxy-fuel combustion for carbon capture and storage in internal combustion engines – A review. Int J Energy Res 2021;46:505–22. http://dx.doi.org/10.1002/er.7199.
[17] Li X, Pei Y, Peng Z, Ajmal T, Rana K-J, Aitouche A, et al. Numerical study on the effects of intake charge on oxy-fuel combustion in a dual-injection spark ignition engine at economical oxygen-fuel ratios. Int J Engine Res 2021;23. http://dx.doi.org/10.1177/14680874211022292.
[18] Van Blarigan A, Kozarac D, Seiser R, Cattolica R, Chen J-Y, Dibble R. Experimental study of methane fuel oxycombustion in a spark-ignited engine. J Energy Resour Technol 2013;136:9. http://dx.doi.org/10.1115/1.4024974.
[19] Kang Z, Wu Z, Zhang Z, Deng J, Hu Z, Li L. Study of the combustion characteristics of a HCCI engine coupled with oxy-fuel combustion mode. SAE Int J Engines 2017;10. http://dx.doi.org/10.4271/2017-01-0649.
[20] Kang Z, Chen S, Wu Z, Deng J, Hu Z, Li L. Simulation study of water injection strategy in improving cycle efficiency based on a novel compression ignition oxy-fuel combustion engine. SAE Int J Engines 2018;11. http://dx.doi.org/10.4271/2018-01-0894.
[21] Gao Y, Li L, Yu X, Deng J, Wu Z. Effect of compression ratio on internal combustion rankine cycle based on simulations. Lect Notes Electr Eng 2015;328:129–38. http://dx.doi.org/10.1007/978-3-662-45043-7_14.
[22] Wu H-W, Wang R-H, Chen Y-C, Ou D-J, Chen T-Y. Influence of port-inducted ethanol or gasoline on combustion and emission of a closed cycle diesel engine. Energy 2013;64. http://dx.doi.org/10.1016/j.energy.2013.11.027.
[23] Zhu S, Hu B, Akehurst S, Copeland C, Lewis A, Yuan H, et al. A review of water injection applied on the internal combustion engine. Energy Convers Manage 2019;184:139–58. http://dx.doi.org/10.1016/j.enconman.2019.01.042.
[24] Perry R. GD. Perry's chemical engineers's handbook eighth edition. McGraw-Hill; 2008.
[25] Serrano JR, Martín J, Gomez-Soriano J, Raggi R. Theoretical and experimental evaluation of the spark-ignition premixed oxy-fuel combustion concept for future CO2 captive powerplants. Energy Convers Manage 2021;244:114498. http://dx.doi.org/10.1016/j.enconman.2021.114498.
[26] Arnau FJ, Novella R, García-Cuevas LM, Gutierrez FA. Adapting an internal combustion engine to oxy-fuel combustion with in-situ oxygen production. In: Internal combustion engine division fall technical conference 2021. 2021, p. 12. http://dx.doi.org/10.1115/ICEF2021-67707.
[27] Portillo E, Alonso-Fariñas B, Vega F, Cano M, Navarrete B. Alternatives for oxygen-selective membrane systems and their integration into the oxy-fuel combustion process: A review. Sep Purif Technol 2019;229:115708. http://dx.doi.org/10.1016/j.seppur.2019.115708.
[28] Wu F, Argyle M, Dellenback P, Fan M. Progress in O_2 separation for oxy-fuel combustion–A promising way for cost-effective CO_2 capture: A review. Prog Energy Combust Sci 2018;67:188–205. http://dx.doi.org/10.1016/j.pecs.2018.01.004.
[29] Arratibel A, Labella A, Liu Y, Porras N, Tanaka D, Annaland M, et al. Mixed ionic-electronic conducting membranes (MIEC) for their application in membrane reactors: A review. Processes 2019;7:128. http://dx.doi.org/10.3390/pr7030128.
[30] Catalán Martínez D, Santafé-Moros M, Gozálvez-Zafrilla J, García Fayos J, Serra J. Characterization of oxygen transport phenomena on BSCF membranes assisted by fluid dynamic simulations including surface exchange. Chem Eng J 2020;387:124069. http://dx.doi.org/10.1016/j.cej.2020.124069.
[31] Valluri S, Claremboux V, Kawatra S. Opportunities and challenges in CO2 utilization. J Environ Sci 2022;113:322–44. http://dx.doi.org/10.1016/j.jes.2021.05.043, URL https://www.sciencedirect.com/science/article/pii/S1001074221002217.
[32] Yadav S, Mondal S. A review on the progress and prospects of oxy-fuel carbon capture and sequestration (CCS) technology. Fuel 2022;308:122057. http://dx.doi.org/10.1016/j.fuel.2021.122057, URL https://www.sciencedirect.com/science/article/pii/S0016236121019335.
[33] Yadav S, Mondal S. Numerical investigation of 660 MW pulverized coal-fired supercritical power plant retrofitted to oxy-coal combustion. Int J Greenh Gas

Control 2021;105:103227. http://dx.doi.org/10.1016/j.ijggc.2020.103227, URL https://www.sciencedirect.com/science/article/pii/S1750583620306526.
[34] Sharma S, Maréchal F. Carbon dioxide capture from internal combustion engine exhaust using temperature swing adsorption. Front Energy Res 2019;7:143. http://dx.doi.org/10.3389/fenrg.2019.00143.
[35] Bilger R, Wu Z. Carbon capture for automobiles using internal combustion rankine cycle engines. J Eng Gas Turbines Power 2009;131:034502. http://dx.doi.org/10.1115/1.3077657.
[36] Munkejord ST, Hammer M, Løvseth S. CO2 transport: data and models – A review. Appl Energy 2016;169:499–523. http://dx.doi.org/10.1016/j.apenergy.2016.01.100.
[37] Redlich O, Kwong J. On the thermodynamics of solutions: An equation of state, fugacities of gaseous solutions. Chem Rev 1949;44:233–44. http://dx.doi.org/10.1021/cr60137a013.
[38] Soave G. Equilibrium constants from a modified Redlich–Kwong equation of state. Chem Eng Sci 1972;27:1197–203. http://dx.doi.org/10.1016/0009-2509(72)80096-4.
[39] Peng D, Robinson D. New two-constant equation of state. Ind Eng Chem Fundam 1976;15. http://dx.doi.org/10.1021/i160057a011.
[40] Li H, Jakobsen J, Wilhelmsen O, Yan J. PVTxy properties of CO2 mixtures relevant for CO2 capture, transport and storage: Review of available experimental data and theoretical models. Appl Energy 2013;88:3567–79. http://dx.doi.org/10.1016/j.apenergy.2011.03.052.
[41] Serrano J, Arnau F, García-Cuevas L, Farias V. Oxy-fuel combustion feasibility of compression ignition engines using oxygen separation membranes for enabling carbon dioxide capture. Energy Convers Manage 2021;247:114732. http://dx.doi.org/10.1016/j.enconman.2021.114732.
[42] Serrano JR, Bracho G, Gomez-Soriano J, Fernandes C. Development of an oxy-fuel combustion system in a compression-ignition engine for ultra-low emissions powerplants using CFD and evolutionary algorithms. Appl Sci 2022;12(14). http://dx.doi.org/10.3390/app12147104, URL https://www.mdpi.com/2076-3417/12/14/7104.
[43] Arnau F, Bracho G, García-Cuevas L, Farias V. A strategy to extend load operation map range in oxy-fuel compression ignition engines with oxygen separation membranes. Appl Therm Eng 2023;226:120268. http://dx.doi.org/10.1016/j.applthermaleng.2023.120268, URL https://www.sciencedirect.com/science/article/pii/S1359431123002971.
[44] Hailong L. Thermodynamic properties of CO2 mixtures and their applications in advanced power cycles with CO2 capture processes [Ph.D. thesis], Stockholm, Sweden: Royal Institute of Technology; 2008.
[45] Metz B, Davidson O, de Coninck H, Loos M, Meyer L. IPCC special report on carbon dioxide capture and storage. Policy Stud 2005.
[46] Bermejo MD, Cocero MJ. Supercritical water oxidation: a technical review. Am Inst Chem Eng J 2006;52(11):3933–51. http://dx.doi.org/10.1002/aic.10993, arXiv:https://aiche.onlinelibrary.wiley.com/doi/pdf/10.1002/aic.10993, URL https://aiche.onlinelibrary.wiley.com/doi/abs/10.1002/aic.10993.
[47] Mangold F, Pilz S, Bjelic S, Vogel F. Equation of state and thermodynamic properties for mixtures of H2O, O2, N2, and CO2 from ambient up to 1000 K and 280 MPa. J Supercrit Fluids 2019;153:104476. http://dx.doi.org/10.1016/j.supflu.2019.02.016.
[48] Smith JM, Van Ness HC, Abbott MM, Swihart MT. Introduction to chemical engineering thermodynamics. Harvard; 2018.
[49] Mathias PM. A versatile phase equilibrium equation of state. Ind Eng Chem Process Des Dev 1983;22(3):385–91. http://dx.doi.org/10.1021/i200022a008.
[50] Sandler SI. Chemical, biochemical and engineering thermodynamics. Harvard; 2016.
[51] Westman S, Stang J, Løvseth S, Austegard A, Snustad I, Ertesvåg I. Vapor-liquid equilibrium data for the carbon dioxide and oxygen (CO2 + O2) system at the temperatures 218, 233, 253, 273, 288 and 298 K and pressures up to 14 MPa. Fluid Phase Equilib 2016;421:67–87. http://dx.doi.org/10.1016/j.fluid.2016.04.002.
[52] Kugel RW. Raoult's law: Binary liquid-vapor phase diagrams: A simple physical chemistry experiment. J Chem Educ 1998;75(9):1125. http://dx.doi.org/10.1021/ed075p1125.
[53] Stephan EF, Hatfield NS, Peoples RS, Pray HA. The solubility of gases in water and in aqueous uranyl salt solutions at elevated temperatures and pressures. 1956, URL https://www.osti.gov/biblio/4379406.
[54] Valtz A, Chapoy A, Coquelet C, Paricaud P, Richon D. Vapour-liquid equilibria in the carbon dioxide-water system, measurement and modelling from 278.2 to 318.2K. Fluid Phase Equilib 2004;226:333–44. http://dx.doi.org/10.1016/j.fluid.2004.10.013.
[55] Müller G, Bender E, Maurer G. Das dampf-flüssigkeitsgleichgewicht des ternären systems ammoniak-kohlendioxid-wasser bei hohen wassergehalten im bereich zwischen 373 und 473 Kelvin. Ber Bunsenges Phys Chem 1988;92(2):148–60. http://dx.doi.org/10.1002/bbpc.198800036, arXiv:https://onlinelibrary.wiley.com/doi/pdf/10.1002/bbpc.198800036, URL https://onlinelibrary.wiley.com/doi/abs/10.1002/bbpc.198800036.
[56] Martín J, Arnau F, Piqueras P, Auñón A. Development of an integrated virtual engine model to simulate new standard testing cycles. In: SAE technical papers vol. 2018-April. 2018, http://dx.doi.org/10.4271/2018-01-1413.
[57] Sanders RE. 9 - Accidents involving compressors, hoses, and pumps. In: Sanders RE, editor. Chemical process safety. 4th ed. Butterworth-Heinemann; 2015, p. 235–67. http://dx.doi.org/10.1016/B978-0-12-801425-7.00009-1, URL https://www.sciencedirect.com/science/article/pii/B9780128014257000091.